Bio-corrosion studies of biodegradable alloys in the Mg-Y-Sr and Mg-Zn-Sr system

by

Li-Fu Hwang

B.S. in Materials Science and Engineering, National Chung Hsing University, 2017

Submitted to the Graduate Faculty of

the Swanson School of Engineering in partial fulfillment

of the requirements for the degree of

Master of Science

University of Pittsburgh

2019

UNIVERSITY OF PITTSBURGH

SWANSON SCHOOL OF ENGINEERING

This thesis was presented

by

Li-Fu Hwang

It was defended on

April 1, 2019

and approved by

Prashant N. Kumta, Ph.D., Professor, Department of Bioengineering

Jung-Kun Lee, Ph.D., Professor, Professor, Department of Mechanical Engineering and Materials Science

Ian Nettleship, Ph.D., Associate Professor, Department of Mechanical Engineering and Materials Science

Thesis Advisor: Prashant N. Kumta, Ph.D., Professor, Department of Bioengineering

Copyright © by Li-Fu Hwang

2019

Bio-corrosion studies of biodegradable alloys in the Mg-Y-Sr and Mg-Zn-Sr system

Li-Fu Hwang, M.S.

University of Pittsburgh, 2019

Pure magnesium possesses similar mechanical properties compared to natural human bone, which helps to avoid the negative effects of stress shielding induced typically by other high modulus bio-inert metallic implants. Magnesium is also considered a biodegradable metal, its degradation *in-vivo* aids in bone regeneration and reduces the need for implant removal surgeries. However, controlling the corrosion rate and reduction of the biotoxicity are the important goals for optimizing Mg alloys for implant application. In this study, Mg-Zn-Sr and Mg-Y-Sr alloys were researched as biodegradable biomedical materials. Zn and Sr are useful alloying elements for refining the grains in Mg alloys. Y serves as an effective solid solution hardener, arising from the large difference in atomic radii between Mg and Y atoms. The two alloys were received our collaborator in India following synthesis using melting followed by squeeze casting. The results of x-ray diffraction patterns and scanning electron microscopy were used to understand the microstructural/composition-functional relationship of the Mg-Zn-Sr and Mg-Y-Sr alloy system. A higher amount of strontium leads to the formation of a secondary $Mg_{17}Sr_2$ phase along the grain boundaries. The corrosion properties of these alloys were analyzed *in-vitro* by immersion and electrochemical tests. The electrochemical corrosion results demonstrated that incorporation of 1 wt% Sr lead to a decrease in corrosion current (I_{corr}) and corrosion rates as compared to pure Mg. Further addition of Sr to the Mg-Zn-Sr and Mg-Y-Sr alloys lead to an increase in corrosion rate due to the presence of higher amounts of secondary phase precipitates. The biomechanical

properties and *in-vitro* cell-toxicities of these alloys should be evaluated in future for their possible applications as a bone fixation device and bone graft.

TABLE OF CONTENTS

PREFACE xi

1.0 INTRODUCTION 1

1.1 Current biomaterials for orthopedic implants 1

1.2 Metals 2

1.3 Polymers 4

1.4 Ceramics 5

1.5 Need for biodegradable metals 6

1.6 Development of biodegradable magnesium 7

1.7 Materials properties of magnesium 7

1.8 Corrosion studies of magnesium 8

1.9 Toxicity and biocompatibility of magnesium alloys 12

1.10 Preferred alloying elements for magnesium-based alloys 12

2.0 THESIS GOALS 15

3.0 MATERIALS AND METHODS 17

3.1 Metallurgical processing of Mg-based alloys 17

3.2 X-ray diffraction 18

3.3 Microstructure analysis 18

3.4 Immersion test 19

3.5 Electrochemical test 20

3.6 Alloy elemental composition analysis 21

4.0 RESULTS 22

4.1 Microstructure and elemental analysis 22

4.2 Immersion experiment 30

4.3 Potentiodynamic polarization (PDP) measurement 40

5.0 DISCUSSION 43

5.1 Microstructure analysis of Mg-Y-Sr and Mg-Zn-Sr alloys 43

5.2 Corrosion behavior of Mg-Y-Sr and Mg-Zn-Sr alloys in HBSS 48

5.3 Corrosion results from Tafel plot 50

6.0 CONCLUSION AND FUTURE WORK 52

BIBLIOGRAPHY 54

LIST OF TABLES

Table 1.1 Summary of the physical and mechanical properties of various implant materials in comparison to natural bone [6] 3

Table 4.1 The nominal chemical compositions of WJ11, WJ14, ZJ11 and ZJ14 alloy..... 29

Table 4.2 The actual chemical compositions of WJ11, WJ14, ZJ11 and ZJ14 alloy 29

Table 4.3 Corrosion rates (mm/year) determined by potentiodynamic polarization and immersion techniques of WJ11, WJ14, ZJ11, ZJ14, AZ31 and pure Mg samples in HBSS..... 42

LIST OF FIGURES

Figure 1.1 Schematic diagram of the ideal change in strength over time of degradable orthopedic implants [14] 9

Figure 1.2 Schematic diagram of the corrosion surface of Mg alloys: (a) the galvanic corrosion between Mg and grain boundaries; (b) the partially protective $Mg(OH)_2$ coating covering the surface of Mg alloys; (c) the reaction of chloride ions to transform $Mg(OH)_2$ into $MgCl_2$; (d) the hydroxyapatite formation by consuming Ca^{2+} and PO_4^{3-}; (e) the particle-shape residues disintegrate from the bulk alloys entering the solution [18] 11

Figure 4.1 XRD patterns of squeezed pure Mg, and WJ11, WJ14, ZJ11 and ZJ14 23

Figure 4.2 SEM image and EDS spectra of (a) WJ11 and (b) WJ14 25

Figure 4.3 SEM image and EDS spectra of (a) ZJ11 and (b) ZJ14 26

Figure 4.4 SEM and optical microscopy image showing surface morphologies after picral acid solution etching 27

Figure 4.5 SEM and optical microscopy image showing surface morphologies after picral acid solution etching 28

Figure 4.6 SEM images and EDS analysis of the particles deposited on the surfaces of (a) WJ11 and (b) WJ14 for 1 day static immersion in HBSS at 37 °C 31

Figure 4.7 SEM images and EDS analysis of the particles deposited on the surfaces of (a) ZJ11 and (b) ZJ14 for 1 day static immersion in HBSS at 37 °C 32

Figure 4.8 EDS analysis of the corrosion product deposited on the surfaces of alloy samples after 7 days immersion in HBSS and SEM images showing surface corrosion after 7, 21, 35 days of static immersion in HBSS at 37 °C 33

Figure 4.9 SEM images and EDS analysis of (a) WJ11 and (b) WJ14 showing surface corrosion morphologies after CrO_3 and $AgNO_3$ treatment for 1 day of static immersion in HBSS at 37 °C 35

Figure 4.10 SEM images and EDS analysis of (a) ZJ11 and (b) ZJ14 showing surface corrosion morphologies after CrO_3 and $AgNO_3$ treatment for 1 day of static immersion in HBSS at 37 °C 36

Figure 4.11 SEM images showing surface corrosion morphologies after CrO_3 and $AgNO_3$ treatment for 7, 21, 35 days of static immersion in HBSS at 37 °C and EDS analysis of alloy samples for 7 days 37

Figure 4.12 pH value of the medium over time during immersion in HBSS 38

Figure 4.13 The weight change of WJ11, WJ14, ZJ11 and ZJ14 after 7, 21, and 35 days immersion in HBSS 39

Figure 4.14 The corrosion rate of WJ11, WJ14, ZJ11 and ZJ14 after 7, 21, and 35 days immersion in HBSS 40

Figure 4.15 Potentiodynamic polarization curves of WJ11, WJ14, ZJ11, ZJ14, AZ31 and pure Mg samples in HBSS 41

Figure 5.1 Mg-Sr binary phase diagram [32] 46

Figure 5.2 Mg-Zn binary phase diagram [32] 47

Figure 5.3 Mg-Y binary phase diagram [32] 48

PREFACE

Firstly, I would like to thank Dr. Prashant N. Kumta for accepting me to be his graduate student. Without his outstanding mentorship and guidance, I would not have completed this research today. He met with me every week and discussed the progress of research whenever he was available. I am also grateful to Dr. Abhijit Roy, John Ohodnicki, Matthew Criado and Dr. Jingyao Wu who always answer my questions and helped me in many ways. When I worked with them, I learned how to design, conduct and perform the scientific research required for me to complete my thesis. Of course, I thank my family who provided financial and spiritual support to me when I pursued the master's degree at the University of Pittsburgh. Finally, I appreciate the Department of Mechanical Engineering and Materials Science and all faculties I have interacted with here at the University of Pittsburgh. I experienced a great journey and colorful graduate student life in Pittsburgh.

1.0 INTRODUCTION

1.1 Current biomaterials for orthopedic implants

Orthopedic fractures are common injuries that are typically caused by accidental loss of balance and collapse, diseases and sports-related accidents, automotive calamities, and occupational injuries. The increasing demand for orthopedic treatments, along with a growing population base, is accelerating the orthopedic devices market demand. The global orthopedic devices market is expected to exceed USD 53 billion by the end of 2024 with the compounded annual growth rate (CAGR) of 3% [1].

During the last 60 years, the evolution of biomaterials research and their clinical availability seemed to be clearly divided into three different generations: bio-inert materials (first generation), bioactive and biodegradable materials (second generation), and materials designs to stimulate specific cellular responses at the molecular level (third generation). The requirement of the first-generation materials was to achieve a suitable combination of physical properties to match those of the host tissue while eliciting the minimal toxic response to the host [2]. The second-generation materials were defined by the development of bioactive materials' ability to strengthen the biological response and tissue bonding, as well as by the development of the bioresorbable materials' ability to undergo a progressive degradation while the new tissue regenerates and heals [2]. The third-generation of materials' goal is to be able to signal and stimulate specific cellular activity and behavior to increase tissue regeneration. These three generations should be interpreted conceptually, not chronologically, because each generation represents the evolution of the requirement and properties of the materials. The materials that each generation brings do not

necessarily replace the use of those of the previous one. First-generation materials are still used in a wide range of medical application. The progress of materials in each generation brings in its own advantages and correspondingly, the advent of third-generation materials will create new possibilities for treatment of orthopedic injuries and other bone tissue related applications [2].

In the clinic, the bone fracture fixation is primary focused on holding the bone fragments together using special implants, such as plates, screws, nails, or wires. On the other hand, bone grafting is required to fill the critical-size defect (CSD) which is typically defined as the minimal defect size beyond the capacity of the natural bone healing process. A bioactive scaffold must not only provide an ideal structure and mechanical stability, but also provide a favorable environment for bone cell regeneration with angiogenesis through the close communication with surrounding tissue [3]. Regardless of the need for bone grafting, use of the appropriate bone fixation devices is critical to maintaining the alignment of bone fragments or bone grafts to fit the defect size, shape and configuration to avoid displacement. Several materials have evolved over the years that have been explored for orthopedic applications. A brief summary is provided below.

1.2 Metals

The synthetic materials systems come from three major classes of biomaterials namely, metals, polymers, and ceramics. The metals have been applied completely for load-bearing applications due to their increased mechanical properties, compared to polymers and ceramics. Conventional metallic implant materials such as titanium (Ti) alloys, stainless steel (SS), and cobalt-chrome (Co-Cr) alloys are commonly used in orthopedic implants due to their outstanding mechanical strength, fracture toughness, elasticity, durability, corrosion resistance, and

biocompatibility. However, use of these orthopedic implants has some limitations and could cause several long-term side effects. The most common problem is the mismatch of mechanical strength of metals to natural bones (see Table 1.1) which can cause stress-shielding effect that results in weakening of the surrounding bone tissue.

In addition, when using current non-degradable metallic biomaterials, a secondary surgery for removal of the implants is often times required. The secondary surgery can lead to an increased risk of infection and potentially results in increased costs and discomfort for the patient. [4]. Furthermore, stainless steel implants have poor wear and corrosion resistance in simulated body fluid (SBF) and release toxic Ni ions within the body. Ti-6Al-4V has been the main titanium alloy used for implants. However, Al is a well-known neurotoxin and could cause dementia, senile dementia, and Alzheimer disease [5]. Hence, there is a need for developing other alloys to provide better clinical care in orthopedic fracture treatment.

Table 1.1 Summary of the physical and mechanical properties of various implant materials in comparison to natural bone [6].

Properties	**Natural bone**	**Magnesium**	**Ti alloy**	**Co–Cr alloy**	**Stainless steel**	**CPC/BVFs**	**PLGA**
Density (g/cm^3)	1.8–2.1	1.74–2.0	4.4–4.5	8.3–9.2	7.9–8.1	3.14	1.3
Elastic modulus (GPa)	3–20	41–45	110–117	230	189–205	35-120	0.2-7
Compressive yield strength (MPa)	130–180	65–100	758–1117	450–1000	170–310	20-900	N/A
Tensile yield strength (MPa)	104-120	100-300	700-900	470-1600	221-1213	3-300	1-27

1.3 Polymers

Besides bio-metals, the biodegradable polymers are widely used clinically for bone tissue engineering applications. Polymers prepared from glycolic acid and lactic acid have found many uses in orthopedic devices. The first application of biodegradable polymers began in the 1960s. Polyglycolide (PGA) is a highly crystalline polymer (45-55% crystallinity) resulting in high tensile modulus (12.5 GPa). The glass transition temperature of the PGA ranges from 35 to 40 °C and the melting point is greater than 200 °C [7]. On the other hand, polylactide (PLA) is a chiral molecule and is synthesized by two optically active forms: L-lactide and D-lactide. PLA is also a crystalline polymer (~37% crystallinity) with high tensile strength, low extension, and high elastic modulus (4.8 GPa). Much of the polymeric research focuses on developing poly (lactide-co-glycolide) polymers (PLGA) for devices and drug-delivery application. The mechanical and degradation properties of the polymeric materials depend on the different ratios of lactide and glycolide [7]. PCL is generally semicrystalline in nature and has an extremely high elongation at breakage (>700%) but a low tensile strength (approximately 23MPa) [7]. The polymer undergoes hydrolytic degradation due to the presence of hydrolytically labile aliphatic ester linkages; however, the rate of degradation is rather slow (2–3 years) [7]. Due to the slow degradation, high permeability to many drugs and minimal toxicity, PCL was initially investigated as a long-term drug delivery vehicle. In addition, due to its excellent biocompatibility, PCL has also been extensively investigated as scaffolds for tissue engineering. Additionally, the biopolymers discussed above do not exhibit any mineralization potential and more importantly, cannot be used for load-bearing applications due to their poor compressive mechanical properties [7].

1.4 Ceramics

The first-generation ceramic biomaterials are alumina, zirconia, calcium phosphate and several porous ceramics. Early application of bioceramics was to replace the traditional metallic femoral heads of hip prostheses with high-density and highly pure alumina. Later, ceramics were used for the acetabular cups, showing excellent wear resistance rates, excellent corrosion resistance, good biocompatibility, and high strength, improving upon the previous polyethylene (PE) cups [2]. Due to excellent biocompatibility and bone-repair properties of calcium phosphate (CaP), calcium phosphate has been used as a bone scaffold or bone void filler (BVF) since the 1970s. The use of porous and bioresorbable scaffolds in the form of bulk sintered ceramics with designed porosity as well as cement formulations that set to form a hard non-porous and porous cement serve as a temporary, three-dimensional scaffold to guide cell attachment, differentiation, proliferation, and subsequent tissue regeneration. Depending on the CaP cement formulation, the setting time, porosity and mechanical properties will be different in these materials [8]. In addition, the majority of calcium phosphate bioceramics is based on hydroxyapatite (HA), β-tricalcium phosphate (β-TCP), α-tricalcium phosphate (α-TCP), and biphasic calcium phosphate (BCP) which is a mixture of either HA+β-TCP or HA+α-TCP. However, any bioceramic made of calcium orthophosphate possesses poor mechanical properties, restricting their use as load-bearing materials (Table 1.1). For instance, the fracture toughness of HA bioceramics does not exceed the value of 1.0 MPa/m^2 (human bone: 2-12 MPa/m^2). Similarly, 45S5 Bioglass®, 45% SiO_2, 24.5% CaO, 24.5% Na_2O and 6% P_2O_5 (wt.%), is the first bioactive glassy material designed to activate genes that stimulate regeneration of living tissues first developed and reported in 1969 by Hench [9]. Due to the high brittleness characteristic of ceramics and glasses, the applications of calcium

phosphate-based bioceramics are focused on primarily, non-load-bearing implants, such as filling of bone defects in oral or orthopedic surgery [10].

1.5 Need for biodegradable metals

As mentioned above, biodegradable polymers are used as fixation devices in the clinical practice for non-load bearing applications as the strength of polymeric materials is lower than human bone (Table 1.1). Another clinical option, calcium phosphate (CaP) bone void fillers (BVF) can adapt bone defects very well; however, they are very brittle in nature and thus are used for non-load bearing applications. Stainless steel, Co, and Ti-based alloys are commonly used commercial bone implants because of their high strength. However, when using these alloys as medical implants, the secondary surgery for implant removal is necessary in the case of implant failure or rejection. Moreover, it could cause various issues such as infection and psychological stress to the patients [4]. In addition, due to serious mismatch of the elastic and tensile strength of the metals and bones, the stress-shielding effect occurs on the surrounding bone, which leads to weakening and even fractures of the surrounding bone. Magnesium and its alloys have evolved in the last decade or so and have emerged as a new class of alloy systems that are biocompatible and degradable as discussed in the next section. These alloys can overcome some of the limitations of permanent metal implants while keeping the advantage of higher stiffness and mechanical properties.

Therefore, the concept of a degradable metallic system, particularly magnesium (Mg) and its alloys, has received considerable attention and considered as important candidates for next-generation bone fixation devices and bone grafts.

1.6 Development of biodegradable magnesium

Research in the field of biodegradable magnesium (Mg) received much attention recently due to the advantage of promoting bone growth while degrading and obviating the need for multiple surgeries. Despite several benefits and progress in the field of Mg alloys for medical application, there is still a need for improvement of biodegradable Mg alloys. Through ionization and hydration reactions with body fluid, Mg-based alloys degrade naturally without creating any local or systemic toxicity. Pure Mg has insufficient strength accompanied by rapid degradation rate which causes the formation of hydrogen gas pockets in the surrounding tissue before the tissues are completely recovered [11]. Much of the research that is being carried out includes controlling the rapid corrosion of Mg and Mg alloys to prevent hydrogen gas evolution and consequently the onset of premature mechanical failure. Therefore, over the past few years, the selection of suitable alloy systems has attracted great attention. Despite the advances made thus far, further studies are still very much needed to control the degradation of Mg implant devices while controlling the mechanical properties to prevent rapid hydrogen gas evolution and premature mechanical failure of the device.

1.7 Materials properties of magnesium

Magnesium has been used for a wide variety of applications, such as military equipment, aircraft, and vehicle components. The low density and lightweight characteristics are the most important factors in the selection of magnesium in these applications. Magnesium has mechanical properties which are comparable to human bone. It is a lightweight metal, with a density of 1.74

g/cm^3, similar to natural bone (1.8-2.1 g/cm^3), and more importantly, much less dense than stainless steel, titanium alloys, and Co-Cr alloys. The fracture toughness of magnesium is greater than ceramics such as HA. The elastic modulus of magnesium (41-45 GPa), compressive yield strength (65-100 MPa) and tensile yield strength (100-300 MPa) are much closer to that of natural bone compared to other metallic implant materials as shown in Table 1.1 [6]. Therefore, magnesium is considered as a good material to mitigate stress shielding effects.

However, compared to other traditional metals, strength, and deformability of magnesium is limited due to its hexagonal close-packed structure (HCP), which indicate a principle slip plane on the (0001) basal plane along the $<11\bar{2}0>$ direction. The second slip occurs in the $<11\bar{2}0>$ on the $\{10\bar{1}0\}$ vertical face planes [12]. To overcome these issues, methods such as grain refinement, work hardening, and solid solution strengthening can improve the strength of the alloys [13].

1.8 Corrosion studies of magnesium

Magnesium and its alloy are susceptible to undergoing degradation in *vivo* relative to other metals as described in section 1.6. This degradation must proceed in a controlled manner so that while the implant is degrading and losing its strength, the load is gradually transferred to the healing bone tissue until the implant diminishes completely once the tissue has fully healed. Figure 1.1 shows that gradual degradation and reduction in mechanical support from the implant occurring with time [14].

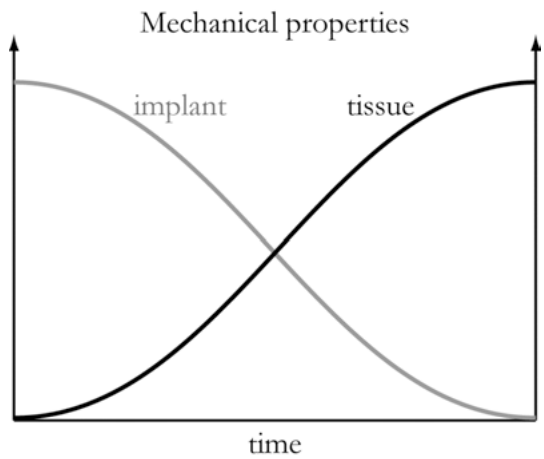

Figure 1.1 Schematic diagram of the ideal change in strength over time of degradable orthopedic implant [14].

When immersed in an aqueous solution, Mg oxidizes to Mg^{2+} and the released electrons in the reaction react with the H^+ ions forming H_2 gas. In addition, Mg^{2+} in turn reacts with hydroxyl ions (OH^-) forming $Mg(OH)_2$ [15]. The overall reaction can be shown as:

$Mg+2H_2O \rightarrow Mg(OH)_2+H_2$

This overall process includes the following partial reactions:

$Mg_{(s)} \rightarrow Mg^{2+}_{(aq)} + 2e^-$ (anodic reaction)

$2H_2O_{(aq)} + 2e^- \rightarrow H_{2\,(g)} + 2OH^-_{(aq)}$ (cathodic reaction)

$Mg^{2+}_{(aq)} + 2OH^-_{(aq)} \rightarrow Mg(OH)_{2\,(s)}$ (product formation)

The standard reduction electrode potential of magnesium (Mg^{2+}/Mg) is -2.37 V at 25°C, which assumes bare metal contact with its divalent ion in the solution. However, the actual

corrosion potential of Mg is usually about -1.7 V in the solution. This means that the bare metal is not in contact with the solution directly. The films of $Mg(OH)_2$ can provide some protection to reduce corrosion [16]. Nevertheless, the layer of porous $Mg(OH)_2$ provides limited protection to completely resist the corrosion encountered in the physiological environment which contains a large number of chloride ions in the order of 150 mmol/l [6]. As $Mg(OH)_2$ reacts with Cl^- to form more soluble $MgCl_2$, it decreases the protected area and promotes the further dissolution of magnesium which causes severe pitting corrosion on Mg. The reactions are summarized as follow [17]:

$$Mg_{(s)} + 2Cl^-_{(aq)} \rightarrow MgCl_{2\,(s)} + 2e^-$$

$$Mg(OH)_{2\,(s)} + 2Cl^-_{(aq)} \rightarrow MgCl_{2\,(s)} + 2OH^-_{(aq)}$$

The undissolved $Mg(OH)_2$ on the surface of the degrading Mg provide favorable sites for hydroxyapatite (HA) nucleation by consuming calcium and phosphate ions from the surrounding fluid. This overall corrosion behavior of polycrystalline Mg alloys in biological solutions is illustrated in Figure1.2 [18].

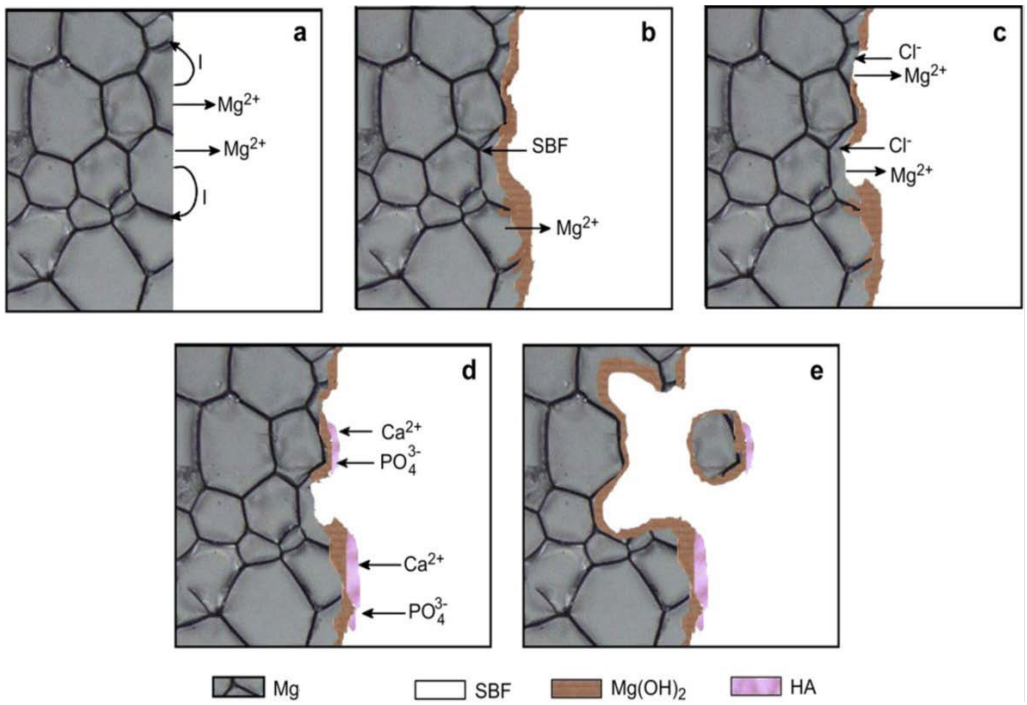

Figure 1.2 Schematic diagram of the corrosion surface of Mg alloys: (a) the galvanic corrosion between Mg and grain boundaries; (b) the partially protective $Mg(OH)_2$ coating covering the surface of Mg alloys; (c) the reaction of chloride ions to transform $Mg(OH)_2$ into $MgCl_2$; (d) the hydroxyapatite formation by consuming Ca^{2+} and PO_4^{3-}; (e) the particle-shape residues disintegrate from the bulk alloys entering the solution [18].

General speaking, potentiodynamic polarization (PDP) response provides information related to relative rates of the anodic and cathodic kinetics for different alloys. The method can also provide corrosion rate from the corrosion current density i_{corr} approximated by a Tafel plot. The shape of the curves in the Tafel plot indicates the form of corrosion that takes place at the

metal surface. For instance, a constant current curve indicates the formation of a passive layer; a symmetric logarithmic curve around the corrosion potential indicates uniform corrosion; pitting or crevice corrosion can also be evaluated based on the shape of the anodic part of the curve after the passive layer has been disrupted [19].

1.9 Toxicity and biocompatibility of Magnesium alloys

Pure Mg has excellent biocompatibility. Mg is the fourth abundant mineral in the human body, containing about 21-28 g of Mg and about 65% in bones and teeth, the remaining 35% is located in the blood, muscle and soft tissues [20]. Generally, an adult requires 320-420 mg of Mg per day. In addition, Mg is also a cofactor of many enzymatic reactions and participate in energy metabolism. The normal range of Mg concentration in adult blood is 0.65-1.05 mmol/l. However, harmful side effects usually occur at a range of Mg of 3.5-5 mmol/l. The symptoms of Mg toxicity include vomiting, nausea, feeling of warmth, flushing, hypotension, bradycardia and other cardiac arrhythmias, somnolence, double vision, slurred speech and weakness [21]. Though these harmful side effects can occur at elevated levels of Mg within the body, *in-vivo* research has shown that Mg implants do not elicit such effects [6].

1.10 Preferred alloying elements for magnesium-based alloys

Pure Mg is not considered as a suitable material for human load bearing applications due to its insufficient mechanical strength and poor corrosion resistance in the physiological

environment. The main purpose of adding alloying elements to Mg is to increase the corrosion resistance and improve the mechanical properties, largely, the ultimate tensile strength, failure strength, and ductility. Biocompatibility is the key factor that limits the selection of a large range of alloying elements in the biological environment. Some alloying elements are largely eliminated from consideration since they are known to be toxic to tissues or cause allergic reactions in the human body [20].

1) Known for toxicity: Ba, Pb, Be, Th, Cd.

2) Known to be allergic: Al, Ce, Cr, Co, Cu, La, Ni, Pr, V.

Previous studies have shown that Ca used as an alloying element in Mg modifies the microstructure and properties of Mg alloys [4]. Furthermore, Ca is an essential component of human bone and can accelerate bone formation [18]. The strengthening effect of Zn is only second to aluminum [22]. The precipitation of an intermetallic phase of Zn and Mg results in a hardening effect [23]. In addition, Zn is considered an essential nutrient, as zinc-deficiency may result in strongly perturbed physiological functions in the human body [22]. Zirconium (Zr) is also used as a grain refiner in magnesium alloy, which contributes to the strength of alloys [24]. In the human body, it has been reported that zirconium, when added in a limited form, shows good biocompatibility and osseointegration *in-vivo* and *in-vitro* [25]. Yttrium (Y) represented by the symbol, W has a high solubility in magnesium and also improves corrosion resistance [17]. In this family, WE43 is one of the most used forms of Mg-Y-RE alloy, and $Mg_{12}YNd$ and $Mg_{14}YNd_2$ are the main precipitated phases. Strontium (Sr) represented by the symbol, J has been also reported as a potential alloying element. Zeng et al. reported that Sr had a significant grain-refinement effect in AZ31 magnesium alloy and could improve both yield strength and elongation of AZ31 alloy [26]. In the perspective of biocompatibility, because of its chemical and physical similarity to Ca,

Sr is also a natural bone-seeking element and about 98% of the total body Sr content is localized in bone tissue [27].

Therefore, in this study, Mg alloys were fabricated containing several alloying elements such as Sr, Y, Ca, Zn, and Zr in different compositions. The goal of this study was to understand the influence of strontium contents on the microstructure and corrosion properties of two different alloy systems, namely, Mg-Y-Sr and Mg-Zn-Sr which also contain Zr added as a grain refiner as discussed above.

2.0 THESIS GOALS

The main goal of this thesis was to understand the influence of strontium contents on the microstructure and corrosion properties of two different alloy systems, namely, Mg-Y-Sr and Mg-Zn-Sr. Sr is known to contribute towards grain refinement. It is also well known that microstructure plays a key role in determining the corrosion and mechanical properties of Mg alloys. Y generally forms more stable corrosion protective film on the surface and serves as an effective solid solution hardener, arising from the large difference in atomic radii between Mg and Y atoms [28]. Zn is an essential element for human body metabolism and also helps to achieve grain refinement. The addition of Sr, Zn and Y as alloying elements to pure Mg will therefore alter the microstructure as well as the corrosion resistance characteristics.

To achieve the above goals two different alloys systems, i.e. Mg-Y-Sr and Mg-Zn-Sr, were designed and synthesized by melting followed by squeeze casting kindly provided by our collaborator, Dr. Partha Saha at the National Institute of Technology, Rourkela, India. The Sr content in these two alloy systems was varied between 1 and 4 wt.%. The synthesized alloys were characterized using x-ray diffraction (XRD), optical microscopy, scanning electron microscopy (SEM), and energy dispersive x-ray spectroscopy (EDS). *In-vitro* immersion corrosion tests were carried out in Hanks Balanced Salt Solution (HBSS) under physiological environment for 1, 7, 21 and 35 days. The weight change was measured during this time and used to calculate the degradation rate (mm/year) according to ASTMG31-72. Potentiodynamic polarization (PDP) measurements were performed in HBSS to further characterize the corrosion characteristics of each alloy. The calculated corrosion potential and current density demonstrated the potential of

the alloys towards corrosion and their corrosion kinetics. The results of these tests aimed to provide useful guide in developing Mg-based alloys for orthopedic applications.

3.0 MATERIALS AND METHODS

3.1 Metallurgical processing of Mg-based alloys

The alloys were synthesized by Dr. Partha Saha, Assistant Professor at the Department of Ceramic Engineering, National Institute of Technology, Rourkela, India. The nominal composition of the alloys were: Mg-1.0 wt.%Zn- 1.0 wt.%Sr- 0.5 wt.% Zr (ZJ11), Mg- 1 wt.%Zn - 4wt.%Sr - 0.5 wt.%Zr (ZJ14), Mg- 1wt.%Sr-1 wt.%Y -0.6 wt.%Ca -0.5 wt.%Zr (WJ11), Mg- 1 wt.%Y - 4wt.%Sr -0.6 wt.%Ca -0.5 wt.%Zr (WJ14) . These alloys were developed using a bottom pouring type stir-casting furnace with a squeeze casting setup. The melting of the materials took place in an electrical resistance furnace using a stainless-steel crucible with a 2.0 kg capacity. The furnace was preheated to a temperature of 750°C. After preheating, the required amount of pure Mg ingots (Minex Metallurgical Co, 99.995%) were first added in the crucible. Next, the stoichiometric amounts of alloying elements/master alloys (China Hunan High Broad New Material Co. Ltd. Hunan, China; Mg-15wt.% Sr, Mg-30wt.% Zr, Mg-30wt.% Y) were added in the liquid melt. As the temperature reached 750 °C, the melt was continuously stirred for 10-15 minutes, ensuring uniform distribution of the alloying elements. Then, the liquid melt was poured at 750 °C using a bottom pouring system into a preheated mild steel cylindrical mold with dimensions of 50 mm diameter and 300 mm length. Once the melt was poured into the mold, an unidirectional ram pressure of 200 MPa was applied on the melt using a vertical hydraulic press of 100-ton capacity for 60 seconds and were air cooled to room temperature. The whole process of fabrication was carried out in a protective atmosphere of 0.5%SF6+Ar (balance) to avoid oxidation and burning.

3.2 X-ray diffraction

In order to evaluate the phases within the Mg-based alloys, x-ray diffraction (XRD) phase analysis was performed using Philips XPERT PRO system employing the Cu K_α (λ=1.54056 Å) radiation source with a Si-detector. X-ray generator was operated at 45kV and 40mA at a 2θ range of 10-80°.

3.3 Microstructure analysis

To observe the microstructure of Mg-based alloys, specimens were mounted in epoxy resin (EpoxiCure, Buehler) and polished with 320, 600, 1200 grit SiC polishing paper and 3μm and 1μm Al_2O_3 powder, respectively, to obtain a mirror finish surface. In order to observe the grain structure of the Mg-based alloys, the samples were then subjected to chemical etching in a picral acid solution consisting of 5 ml acetic acid, 6 g picric acid, 10 ml water, and 100 ml ethanol followed by using acetone to clean the surface. The polished and etched surface was observed using an optical microscope (Smartzoom 5, Zeiss, Germany) to obtain the optical microstructure images. The microstructure and precipitates of alloys surface were also observed under the scanning electron microscope (Apreo SEM, Thermo Fisher Scientific). The elemental composition and distribution were analyzed by energy dispersive x-ray spectroscopy (Elite T EDS system, EDAX).

3.4 Immersion test

Squeeze casted WJ11, WJ14, ZJ11, ZJ14 alloys, which were synthesized by Dr. Partha Saha were prepared into cylindrical specimens with a diameter of 10 mm and thickness of 1 mm for conducting the immersion test, the electrochemical test, and other characterization analyses. The surface of the samples were polished with 320, 600, 1200 grit SiC polishing paper, respectively. All polished samples were ultrasonically cleaned in acetone for 15 minutes and then air dried at room temperature. Polished samples were stored in a desiccator until further testing and characterization. Surface area and the weight of each sample was measured before the immersion test. These samples were immersed in 20 ml of Hank's Balanced Salt Solution (HBSS) per cm^2 of alloy as during the entire span of the measurement. For statistical analysis of magnesium alloy corrosion, 3 samples were used (n= 3) per time point. Immersed samples were kept inside an incubator at 37°C for 7, 21 and 35 days. The immersed samples were removed from the HBSS media at each time point and dried at room temperature. To measure the weight loss, the corrosion products on the surface of the samples were removed by immersing in a chromic acid solution (200 g/l of chromic acid and 10 g/l of silver nitride ($AgNO_3$)) for 1 minute, rinsed with acetone and dried at room temperature. The average and standard deviation were calculated for each group. The corrosion rate was calculated according to ASTM G31-72 by the following equation:

$$\boldsymbol{C = \frac{K \cdot W}{A \cdot T \cdot \rho}} \qquad \text{Equation 3-1}$$

where C is the corrosion rate in mm $year^{-1}$ (mmpy), the constant K is $8.76*10^4$, W is the mass loss in grams, A is the sample area exposed to solution in cm^2, T is the time of exposure in h, and ρ is the density of the material in g/cm^3. The pH value of the solution was also recorded in the immersion test. Average and standard deviations were reported.

3.5 Electrochemical test

The corrosion potential and current density of Mg alloys were determined by potentiodynamic polarization (PDP) scanning using an electrochemical analyzer system (CHI 604A, CH Instruments, Inc., Austin, TX). Each polished cylindrical sample was connected to a copper wire with silver epoxy and mounted in epoxy resin. The mounted samples were re-polished using 1200 grit silicon paper, sonicated in isopropanol, and dried in air. 125ml of fresh HBSS was used as an electrolytic solution for each test. An Ag/AgCl electrode, platinum electrode, and the sample were connected as the reference, counter, and the working electrode respectively. Prior to testing the HBSS was heated to 37°C and maintained at this temperature during the course of the test. The open circuit potential (OCP) analysis was performed over a 30 minutes timeframe. Potentiodynamic polarization tests were conducted at a scanning rate of 0.001 V/s and a potential window of 200mV above and 500mV below the OCP. To determine corrosion potential (E_{corr}) and corrosion current density (I_{corr}), Tafel plot was extrapolated linearly from the anodic and cathodic branch. The corrosion rate was calculated by the following equation:

$$\boldsymbol{C_{corr}} = \frac{\boldsymbol{I_{corr} \cdot K \cdot EW}}{\boldsymbol{\rho \cdot A}} \qquad \text{Equation 3-2}$$

where C is the corrosion rate in mmpy, I_{corr} is the corrosion current density in $\mu A/cm^2$, the constant K is $3.272*10^{-2}$, EW is the equivalent weight in g/equivalent, ρ is the density of the material in g/cm^3, A is the area of the material in cm^2.

3.6 Alloy elemental composition analysis

The experimental elemental composition of each alloy was analyzed by inductively coupled plasma-optical emission spectroscopy (ICP-OES, iCAP duo 6500 Thermo Fisher, Waltham, MA). Samples were prepared by dissolving 100mg of each alloy in 40 ml of dilute nitric acid. A standard calibration curve was generated by using elemental standards diluted in 3% nitric acid to the desired concentration range (1 ppm-100 ppm). The standard calibration curve was used to calibrate the ppm of each sample.

4.0 RESULTS

4.1 Microstructure and elemental analysis

The XRD patterns of the squeeze casted Mg alloys are shown in Figure 4.1. All the alloys mainly consist of single-phase Mg. Both the WJ11 and ZJ11 show only the presence of hexagonal α-Mg and the absence of any other crystalline phase. However, with the increase in the concentration of strontium in WJ14 and ZJ14, a crystalline phase of $Mg_{17}Sr_2$ was present in addition to α -Mg phase.

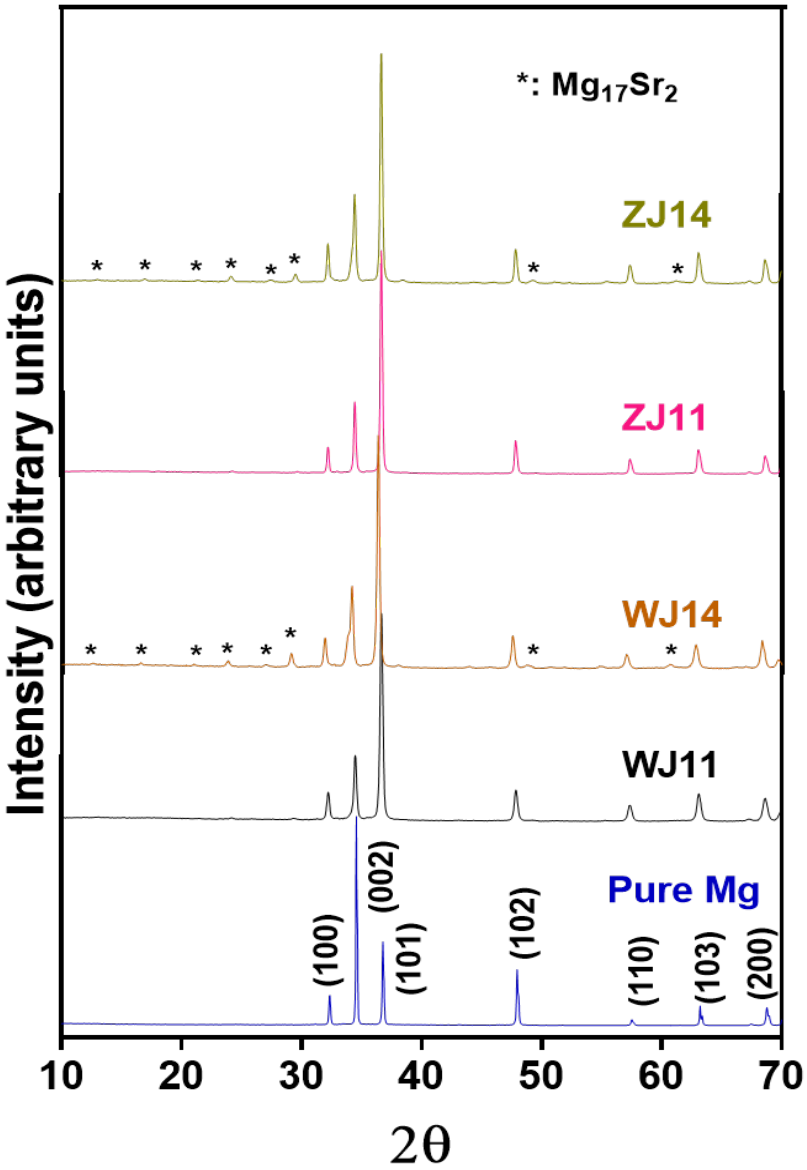

Figure 4.1 XRD patterns of squeezed pure Mg, and WJ11, WJ14, ZJ11 and ZJ14.

Figure 4.2 and 4.3 show the SEM and EDX of the Mg-Y-Sr and Mg-Zn-Sr alloys respectively. Figure 4.4 and 4.5 show the optical micrographs of all the squeeze casted alloys. From Figure 4.2 and 4.3, there were two main phases in the squeeze cast samples. The matrix indicates α–phase and the dendritic precipitates along the grain boundaries revealed the presence of intermetallic phases. An increase in precipitate was observed with the increase in Sr. WJ11 alloy showed the presence of Sr along the grain boundaries (Figure 4.2a position B). The grain size of WJ11 was 48.71 ± 5.73 μm. An increase in the Sr content to 4 wt.% did not seem to change the composition of the solid solution or precipitates much (Figure 4.2b position C). Nevertheless, an increasing amount of second phase areas were observed (Figure 4.2b). The grain size of the WJ14 alloy was 30.91 ± 5.83 μm. Sr addition to the Mg-Zn system also presented a similar effect on the precipitates (Figure 4.3a, b). The grain size of ZJ11 and ZJ14 alloy were 57.21 ± 9.3 μm and 35.5 ± 2.65 μm, respectively.

The alloy nominal and actual compositions determined by inductively coupled plasma optical emission spectroscopy, are listed in Table 4.1 and 4.2. WJ11 alloy consisted of approximately 97.9% Mg, 0.83% Sr, and 0.86% Y in actual, which is similar to design composition 96.9% Mg, 1% Sr and 1% Y. WJ14 alloy consisted of approximately 95.58% Mg, 3.25% Sr, and 0.81% Y, which is closed to design composition 93.9% Mg, 4% Sr and 1% Y. ZJ11 alloy consisted of approximately 98.29% Mg, 0.82% Zn, and 0.87% Sr, which is similar to design composition 97.5% Mg, 4% Sr and 1% Zn. ZJ14 alloy consisted of approximately 95.77% Mg, 0.78% Zn, and 3.40% Sr, which is similar to design composition 94.5% Mg, 4% Sr and 1% Zn. These results indicate that the alloys were correctly produced in accordance with the concentration of added elements.

<table>
<tr><th></th><th>SEM</th><th>EDS</th></tr>
<tr><td>WJ11</td><td>(a)
 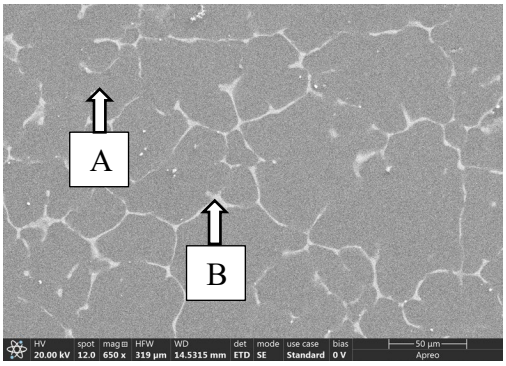
</td><td>
<table>
<tr><th>Element (wt.%)</th><th>Position A</th><th>Position B</th><th>Overall</th></tr>
<tr><td>Mg K</td><td>100.00</td><td>85.02</td><td>99.37</td></tr>
<tr><td>Sr L</td><td>-</td><td>11.69</td><td>0.32</td></tr>
<tr><td>Y L</td><td>-</td><td>-</td><td>0.1</td></tr>
<tr><td>Ca K</td><td>-</td><td>3.28</td><td>0.2</td></tr>
</table>
</td></tr>
<tr><td>WJ14</td><td>(b)
 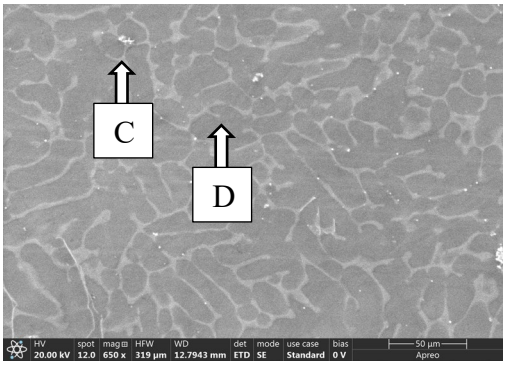
</td><td>
<table>
<tr><th>Element (wt.%)</th><th>Position C</th><th>Position D</th><th>Overall</th></tr>
<tr><td>Mg K</td><td>84.66</td><td>100.00</td><td>96.51</td></tr>
<tr><td>Sr L</td><td>15.34</td><td>-</td><td>2.25</td></tr>
<tr><td>Y L</td><td>-</td><td>-</td><td>0.32</td></tr>
<tr><td>Ca K</td><td>-</td><td>-</td><td>0.9</td></tr>
</table>
</td></tr>
</table>

Figure 4.2 SEM image and EDS spectra of (a) WJ11 and (b) WJ14.

ZJ11

(a)

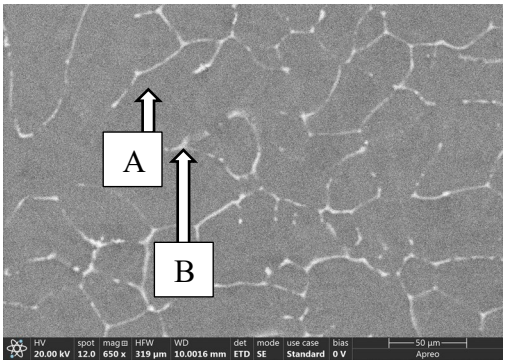

Element (wt.%)	Position A	Position B	Overall
Mg K	100.00	84.48	98.21
Sr L	-	9.98	0.97
Zn K	-	5.54	0.82

ZJ14

(b)

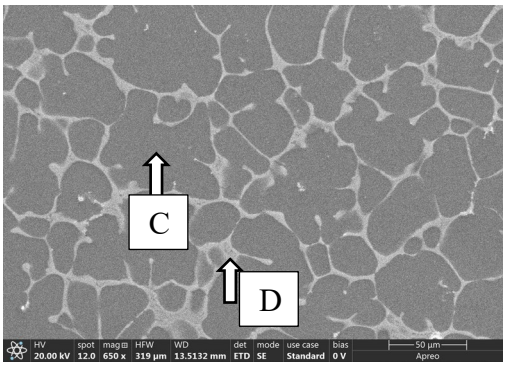

Element (wt.%)	Position C	Position D	Overall
Mg K	100	82.94	96.99
Sr L	-	17.06	1.99
Zn K	-	-	0.97
Zr L	-	-	0.05

Figure 4.3 SEM image and EDS spectra of (a) ZJ11 and (b) ZJ14.

	SEM	Optical microscopy
WJ11	(a) 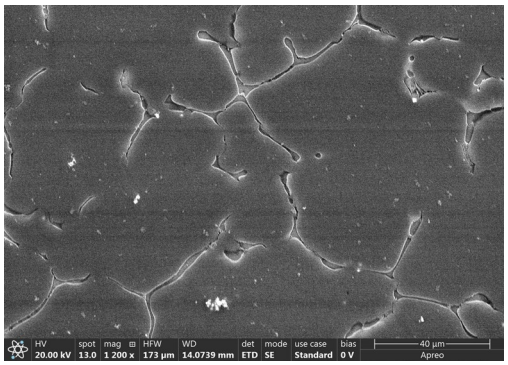	(b) 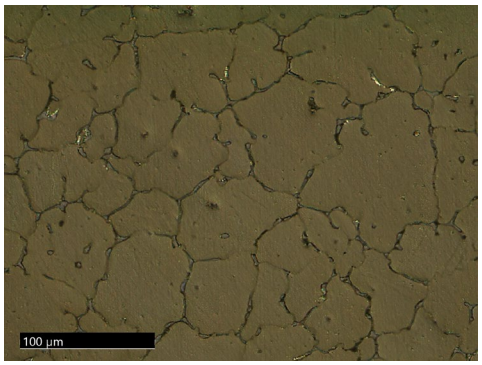
WJ14	(c) 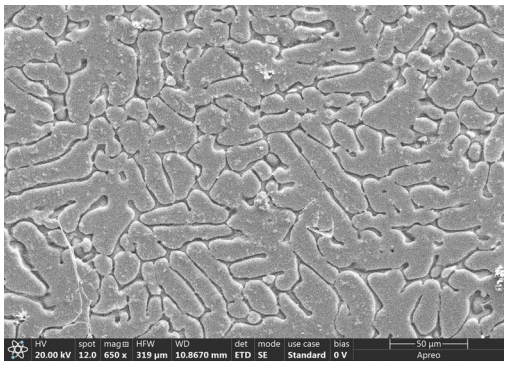	(d) 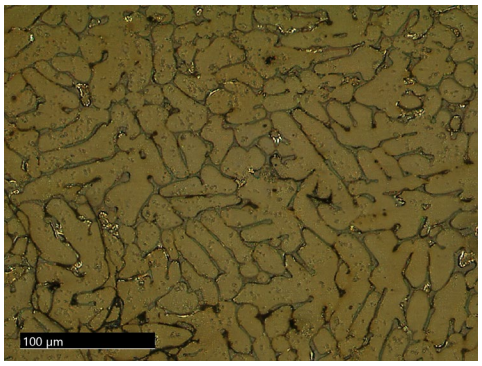

Figure 4.4 SEM and optical microscopy image showing surface morphologies after picral acid solution etching.

ZJ11	(a) 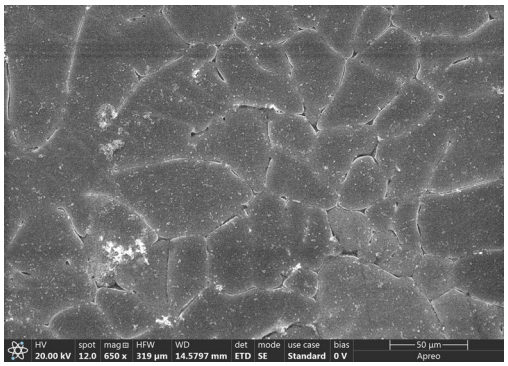 	(b) 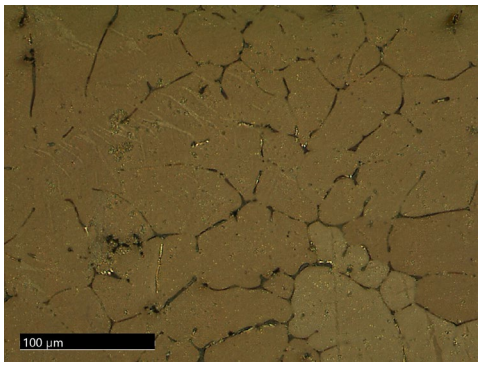
ZJ14	(c) 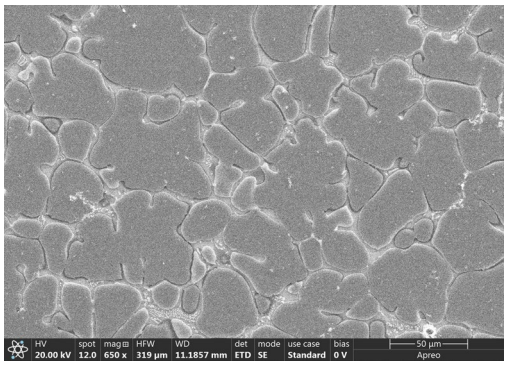 	(d) 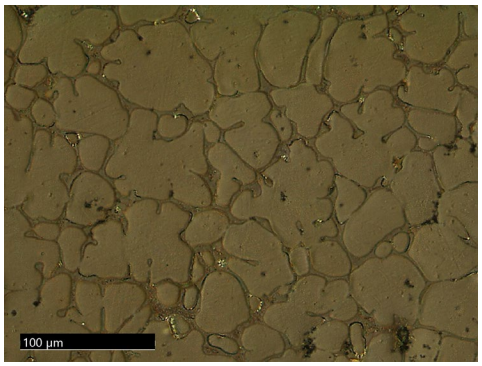

Figure 4.5 SEM and optical microscopy image showing surface morphologies after picral acid solution etching.

Table 4.1 The nominal chemical compositions of WJ11, WJ14, ZJ11 and ZJ14 alloy.

Alloy (wt.%)	Mg	Zn	Sr	Zr	Ca	Y
WJ11	96.9%	-	1%	0.5%	0.6%	1%
WJ14	93.9%	-	4%	0.5%	0.6%	1%
ZJ11	97.5%	1%	1%	0.5%	-	-
ZJ14	94.5%	1%	4%	0.5%	-	-

Table 4.2 The actual chemical compositions of WJ11, WJ14, ZJ11 and ZJ14 alloy.

Alloy (wt.%)	Mg	Zn	Sr	Zr	Ca	Y
WJ11	97.90%	-	0.83%	0.11%	0.30%	0.86%
WJ14	95.58%	-	3.25%	0.02%	0.35%	0.81%
ZJ11	98.29%	0.82%	0.87%	0.01%	-	-
ZJ14	95.77%	0.78%	3.40%	0.05%	-	-

4.2 Immersion experiment

In order to understand the effect of Sr in Mg-Y-Sr and Mg-Zn-Sr alloys in HBSS, the immersion tests were performed. The corrosion characteristics of the Mg-Y-Sr and Mg-Zn-Sr alloys were initially monitored by immersing the samples for 1, 7, 21 and 35 days in HBSS. Figure 4.6 and 4.7 show the formation of the oxide layer, micro-pores and pits on the surface after 1 day of immersion in HBSS for all alloys. Figure 4.8 a, b and c present the SEM images of the WJ11, ZJ11, and ZJ14 immersed in the HBSS for 7 days. All of the alloy surfaces exhibited the presence of a cracked oxide layer. In WJ11, ZJ11 and ZJ14 pitting corrosion can be observed, with the largest pits observed in ZJ14 (Figure 4.8). In the case of WJ14 alloy, the immersed samples degraded too fast and disintegrated into fragments within 7 days exposure to the HBSS, therefore no images could be taken. EDS results showed that areas on WJ11 samples were rich in O and Mg, and a limited amount of P, Cl and Ca were present (Figure 4.8a). For Mg-Zn-Sr system, EDS results showed that ZJ11 and ZJ14 surfaces were rich in oxygen and magnesium, and a small amount of C, Sr, P, Cl, Ca and Zn were present. The content of strontium on ZJ11 sample was less than that of ZJ14 sample. Figure 4.8d, e and f present the secondary electron images of the alloy samples immersed in the HBSS for 21 days. In the figure, all of the alloy samples were covered with a large amount of white precipitates. At high magnification, both ZJ11 and ZJ14 demonstrated the multilayer of corrosion product and many deep pits (Figure 4.8e and f). Figure 4.8g and h present the secondary electron SEM images of the alloy samples immersed in the HBSS for 35 days and ZJ14 alloy samples were fully covered by corrosion product. The presence of filiform and irregularly shaped film was observed at high magnification (Figure 4.8h). Additionally, the various ions present within the corrosion products of all the alloys are similar to what has been observed in other work pertaining to immersion tests of Mg based alloys within HBSS [18, 29].

<table>
<tr><th></th><th>SEM</th><th>EDS</th></tr>
<tr><td>WJ11</td><td>(a)
 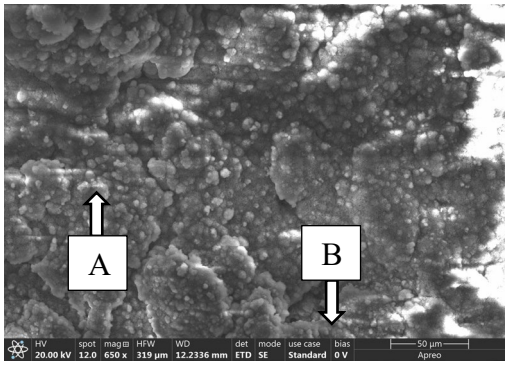
</td><td>
<table>
<tr><th>Element (wt.%)</th><th>Position A</th><th>Position B</th><th>Overall</th></tr>
<tr><td>C K</td><td>-</td><td>-</td><td>0.86</td></tr>
<tr><td>O K</td><td>51.05</td><td>53.15</td><td>51.02</td></tr>
<tr><td>Mg K</td><td>48.95</td><td>46.85</td><td>47.11</td></tr>
<tr><td>P K</td><td>-</td><td>-</td><td>0.07</td></tr>
<tr><td>Cl K</td><td>-</td><td>-</td><td>0.57</td></tr>
<tr><td>Ca K</td><td>-</td><td>-</td><td>0.33</td></tr>
</table></td></tr>
<tr><td>WJ14</td><td>(b)
 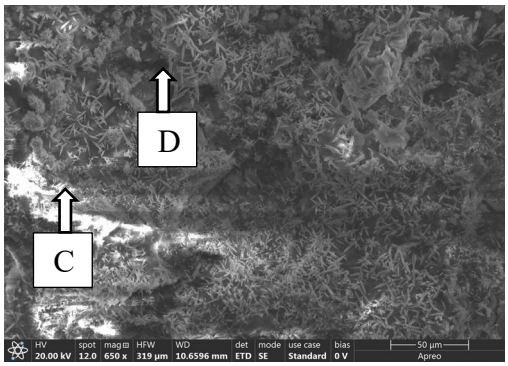
</td><td>
<table>
<tr><th>Element (wt.%)</th><th>Position C</th><th>Position D</th><th>Overall</th></tr>
<tr><td>C K</td><td>-</td><td>-</td><td>0.97</td></tr>
<tr><td>O K</td><td>40.61</td><td>9.13</td><td>30.47</td></tr>
<tr><td>Mg K</td><td>55.27</td><td>90.87</td><td>34.30</td></tr>
<tr><td>Sr L</td><td>4.12</td><td>-</td><td>32.01</td></tr>
<tr><td>P K</td><td>-</td><td>-</td><td>0.08</td></tr>
<tr><td>Cl K</td><td>-</td><td>-</td><td>0.12</td></tr>
<tr><td>Ca K</td><td>-</td><td>-</td><td>2.04</td></tr>
</table></td></tr>
</table>

Figure 4.6 SEM images and EDS analysis of the particles deposited on the surfaces of (a) WJ11 and (b) WJ14 for 1 day static immersion in HBSS at 37 °C.

ZJ11

(a)

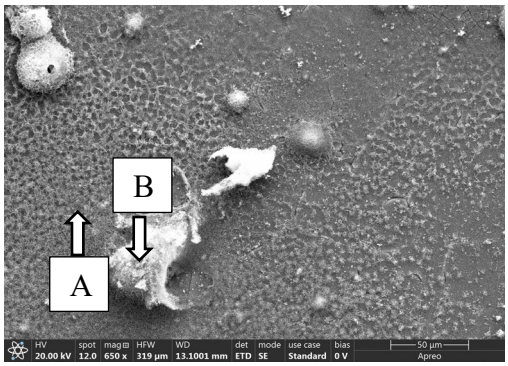

Element (wt.%)	Position A	Position B	Overall
C K	-	-	0.21
O K	5.35	49.62	8.72
Mg K	91.23	50.38	81.21
Sr L	-	-	0.10
P K	1.32	-	3.15
Cl K	-	-	0.13
Ca K	2.10	-	6.09
Zn K	-	-	0.40

ZJ14

(b)

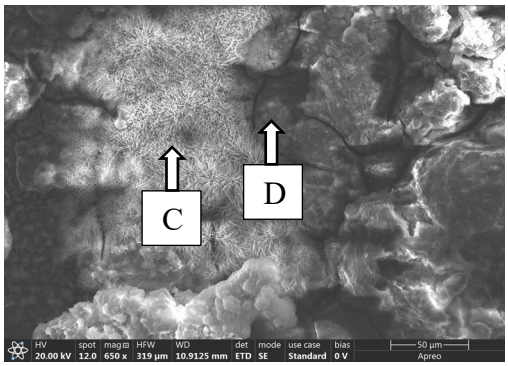

Element (wt.%)	Position C	Position D	Overall
C K	-	-	0.81
O K	36.07	45.39	41.85
Mg K	38.63	37.98	38.80
Sr L	-	-	0.1
P K	-	3.74	1.59
Cl K	25.31	7.01	14.3
Ca K	-	5.89	2.18
Zn K	-	-	0.38

Figure 4.7 SEM images and EDS analysis of the particles deposited on the surfaces of (a) ZJ11 and (b) ZJ14 for 1-day static immersion in HBSS at 37 °C.

	WJ11	ZJ11	ZJ14
7 days	(a) 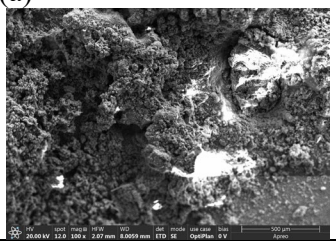	(b) 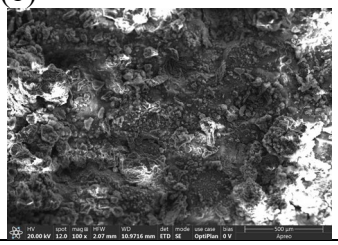	(c) 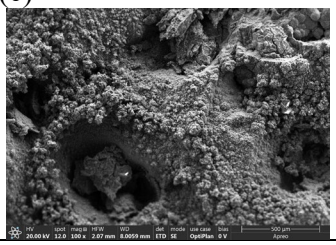
21 days	(d) 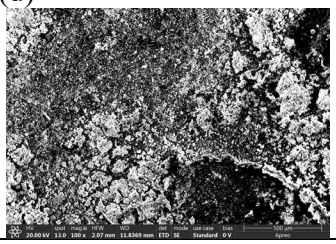	(e) 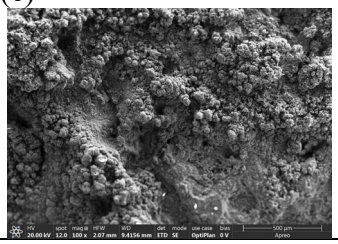	(f) 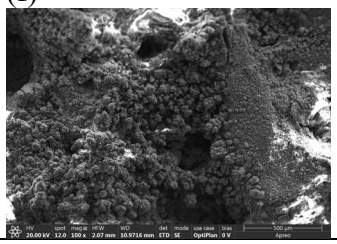
35 days	(g) 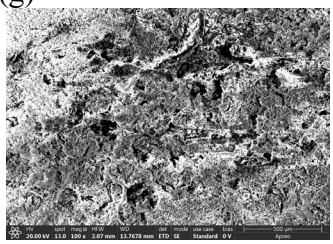		(h) 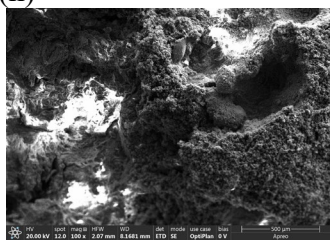
EDS			

Element (wt.%)	WJ11	ZJ11	ZJ14
C K	-	0.9	0.41
O K	49.02	50.07	50.9
Mg K	44.79	43.19	45.31
Sr L	-	0.05	0.43
P K	1.43	1.01	0.01
Cl K	0.6	2.08	1.27
Ca K	4.16	1.85	0.72
Zn K	-	0.85	0.95

Figure 4.8 EDS analysis of the corrosion product deposited on the surfaces of alloy samples after 7 days immersion in HBSS and SEM images showing surface corrosion after 7, 21, 35 days of static immersion in HBSS at 37 °C.

Figure 4.9 and 4.10 show the alloy surface after removal of the corrosion products using a CrO_3 and $AgNO_3$ solution of all the alloys. The presence of interconnected pits along the grain boundaries was observed on the corroded surface among all Mg alloys (Figure 4.9 and 4.10). The weight % of Sr present on the corded samples decreased compared to the uncorroded alloy samples. Figure 4.11 shows that with the longer time of immersion in HBSS, the number of pits and the area of corrosion increase on the surface.

<table>
<tr><th></th><th>SEM</th><th>EDS</th></tr>
<tr><td>WJ11</td><td>(a)
 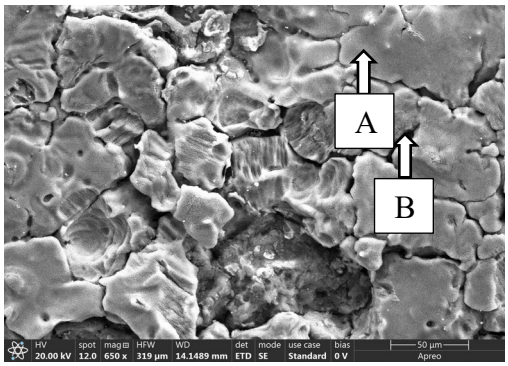
</td><td>
<table>
<tr><th>Element (wt.%)</th><th>Position A</th><th>Position B</th><th>Overall</th></tr>
<tr><td>O K</td><td>8.887</td><td>-</td><td>10.12</td></tr>
<tr><td>Mg K</td><td>84.83</td><td>35.16</td><td>83.65</td></tr>
<tr><td>Sr L</td><td>-</td><td>-</td><td>0.03</td></tr>
<tr><td>Y L</td><td>-</td><td>-</td><td>0.59</td></tr>
<tr><td>Ca K</td><td>-</td><td>-</td><td>0.16</td></tr>
<tr><td>Cr K</td><td>6.3</td><td>64.84</td><td>5.45</td></tr>
</table></td></tr>
<tr><td>WJ14</td><td>(b)
 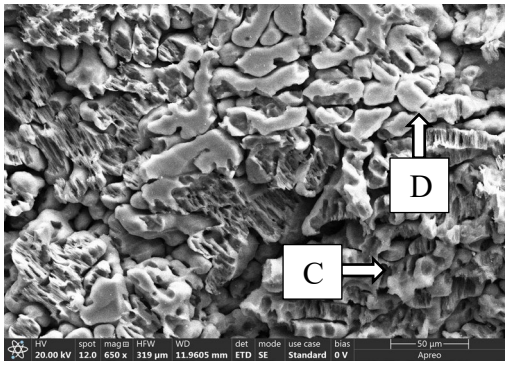
</td><td>
<table>
<tr><th>Element (wt.%)</th><th>Position C</th><th>Position D</th><th>Overall</th></tr>
<tr><td>O K</td><td>-</td><td>-</td><td>2.75</td></tr>
<tr><td>Mg K</td><td>100.00</td><td>100.00</td><td>93.98</td></tr>
<tr><td>Sr L</td><td>-</td><td>-</td><td>0.07</td></tr>
<tr><td>Y L</td><td>-</td><td>-</td><td>0.35</td></tr>
<tr><td>Ca K</td><td>-</td><td>-</td><td>0.47</td></tr>
<tr><td>Cr K</td><td>-</td><td>-</td><td>2.87</td></tr>
</table></td></tr>
</table>

Figure 4.9 SEM images and EDS analysis of (a) WJ11 and (b) WJ14 showing surface corrosion morphologies after CrO_3 and $AgNO_3$ treatment for 1 day of static immersion in HBSS at 37 °C.

ZJ11

(a)

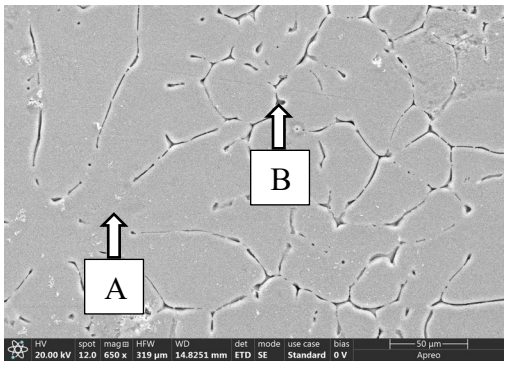

Element (wt.%)	Position A	Position B	Overall
Mg K	100.00	100.00	99.42
Sr L	-	-	0.1
Zn K	-	-	0.48

ZJ14

(b)

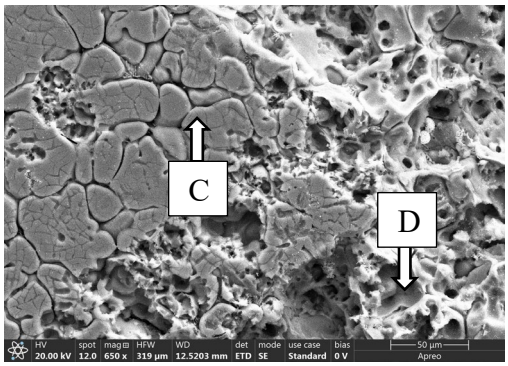

Element (wt.%)	Position C	Position D	Overall
Mg K	100.00	100.00	98.86
Sr L	-	-	0.4
Zn K	-	-	0.75

Figure 4.10 SEM images and EDS analysis of (a) ZJ11 and (b) ZJ14 showing surface corrosion morphologies after CrO_3 and $AgNO_3$ treatment for 1 day of static immersion in HBSS at 37 °C.

	WJ11	ZJ11	ZJ14
7 days	(a) 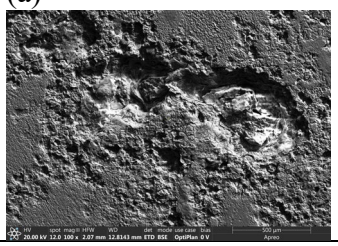	(b) 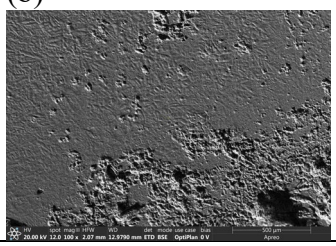	(c) 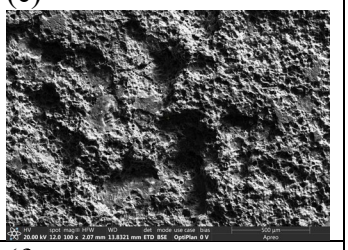
21 days	(d) 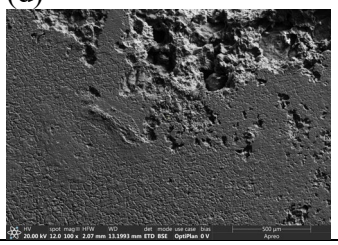	(e) 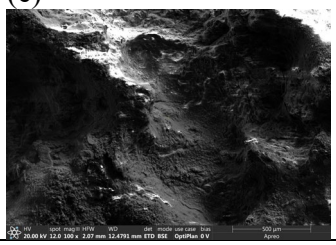	(f) 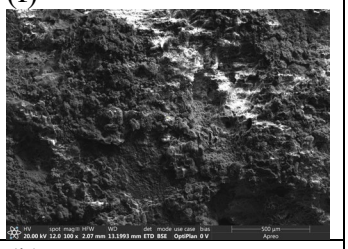
35 days	(g) 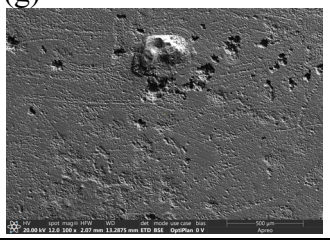		(h) 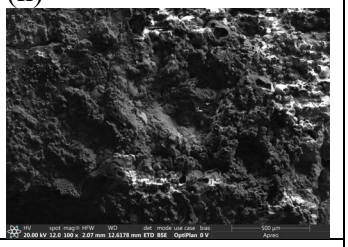
EDS			

Element (wt.%)	WJ11	ZJ11	ZJ14
C K	-	2.17	-
O K	10.06	8.6	13.66
Mg K	84.51	81.3	76.17
Sr L	-	0.16	2.3
Y L	0.38	-	-
P K	1.27	0.69	0.46
Cl K	-	0.04	-
Cr K	3.78	4.99	5.32
Zn K	-	2.06	2.1

Figure 4.11 SEM images showing surface corrosion morphologies after CrO_3 and $AgNO_3$ treatment for 7, 21, 35 days of static immersion in HBSS at 37 °C and EDS analysis of alloy samples for 7 days.

Figure 4.12 shows the pH value of the immersion solution as a function of immersion time. The pH value of HBSS at 37 °C is 7.6. The highest pH value was observed in the WJ14 alloy after 1 week because it fully degraded. On the other hand, the pH values of the rest of the alloys were very similar at each time point (Figure 4.12).

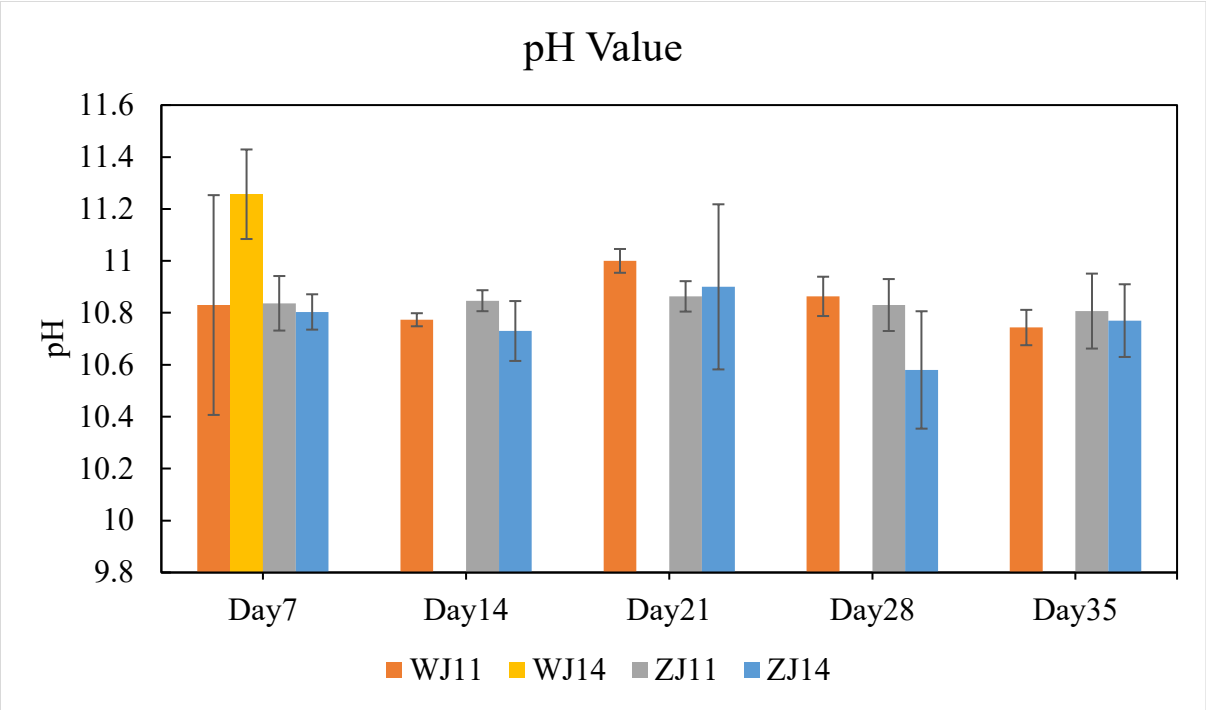

Figure 4.12 pH value of the medium over time during immersion in HBSS.

The average weight change of ZJ11, ZJ14, WJ11, WJ14 alloys in HBSS for 7, 21 and 35 days were displayed in Figure 4.13. WJ14 completely degraded within 7 days of immersion. As the immersion time became longer, the values of weight change were larger in each of the alloys. Figure 4.14 shows that the corrosion rate of WJ11 increased slightly after 21 and 35 days. Whereas ZJ11 and ZJ14 showed no change in corrosion rates during the immersion test.

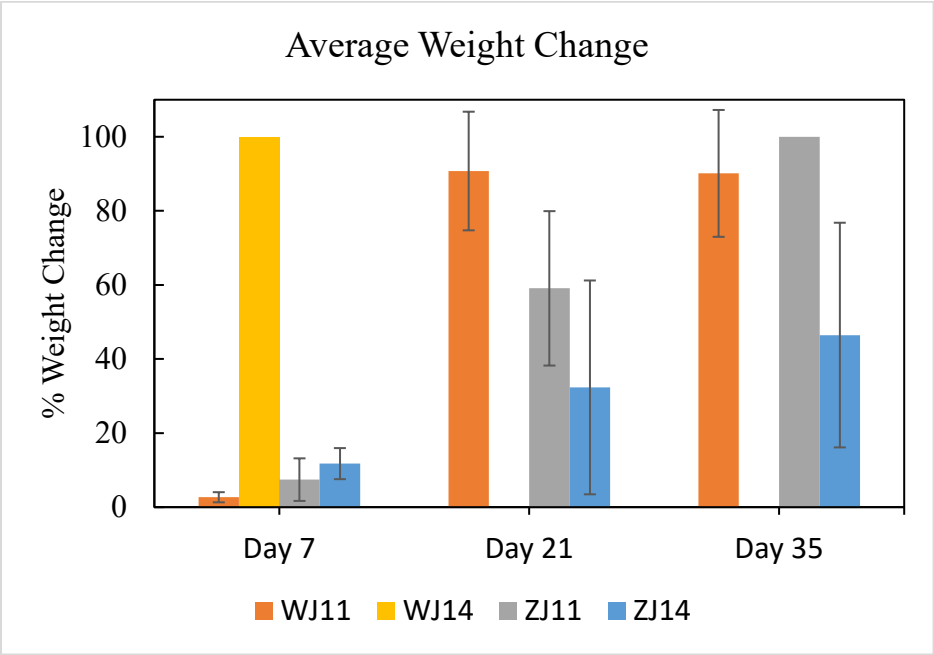

Figure 4.13 The weight change of WJ11, WJ14, ZJ11 and ZJ14 after 7, 21, and 35 days immersion in HBSS.

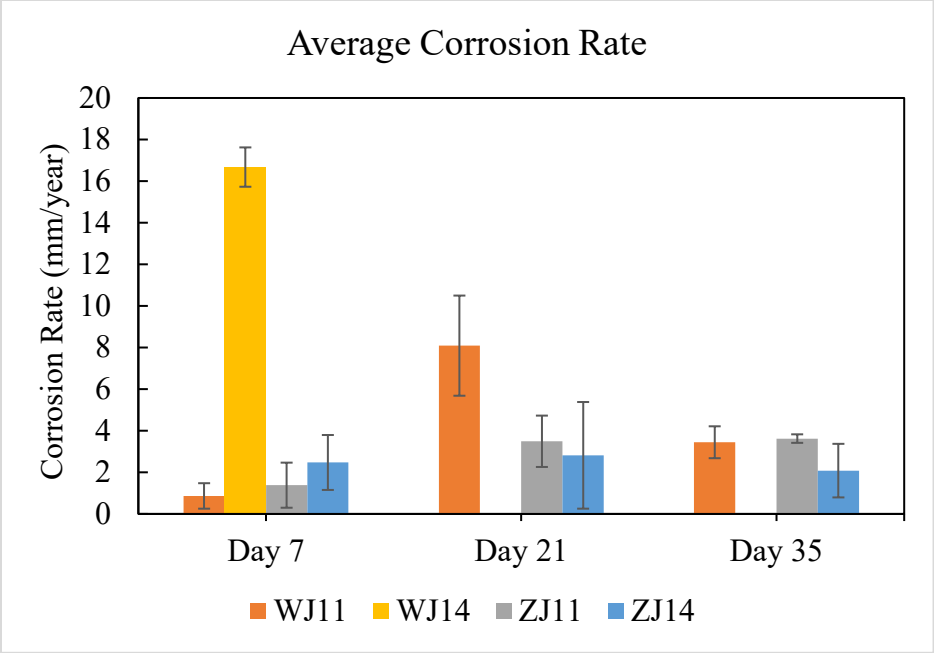

Figure 4.14 The corrosion rate of WJ11, WJ14, ZJ11 and ZJ14 after 7, 21, and 35 days immersion in HBSS.

4.3 Potentiodynamic polarization (PDP) measurement

In order to further characterize the effect of Sr on the Mg-Zn-Sr and Mg-Y-Sr alloy systems, potentiodynamic polarization tests were performed. The potentiodynamic polarization curves for the corrosion of Mg alloys in HBSS are shown in Figure 4.15 and Table 4.1 shows the corrosion potential (E_{corr}), corrosion current (I_{corr}) and electrochemical corrosion rates (CRE_{corr}). The electrochemical corrosion of pure Mg and AZ31 data were obtained from previous studies in

our group. The current density (I_{corr}) of WJ11, WJ14, ZJ11, and ZJ14 were 1.41 ± 0.45, 5.63 ± 7.33, 0.69 ± 0.06 and 5.98 ± 6.78 μA/cm^2, respectively. The results indicate that the corrosion current increases with an increase in Sr content in the alloys, and ZJ11 has the lowest I_{corr} value. The largest calculated I_{corr} and CR_{corr} were observed from ZJ14 and were 5.98 ± 6.78 μA/cm^2 and 1.29 ± 1.46 mm/year, respectively. Interestingly, the standard deviations for alloys containing larger amounts of Sr were very high.

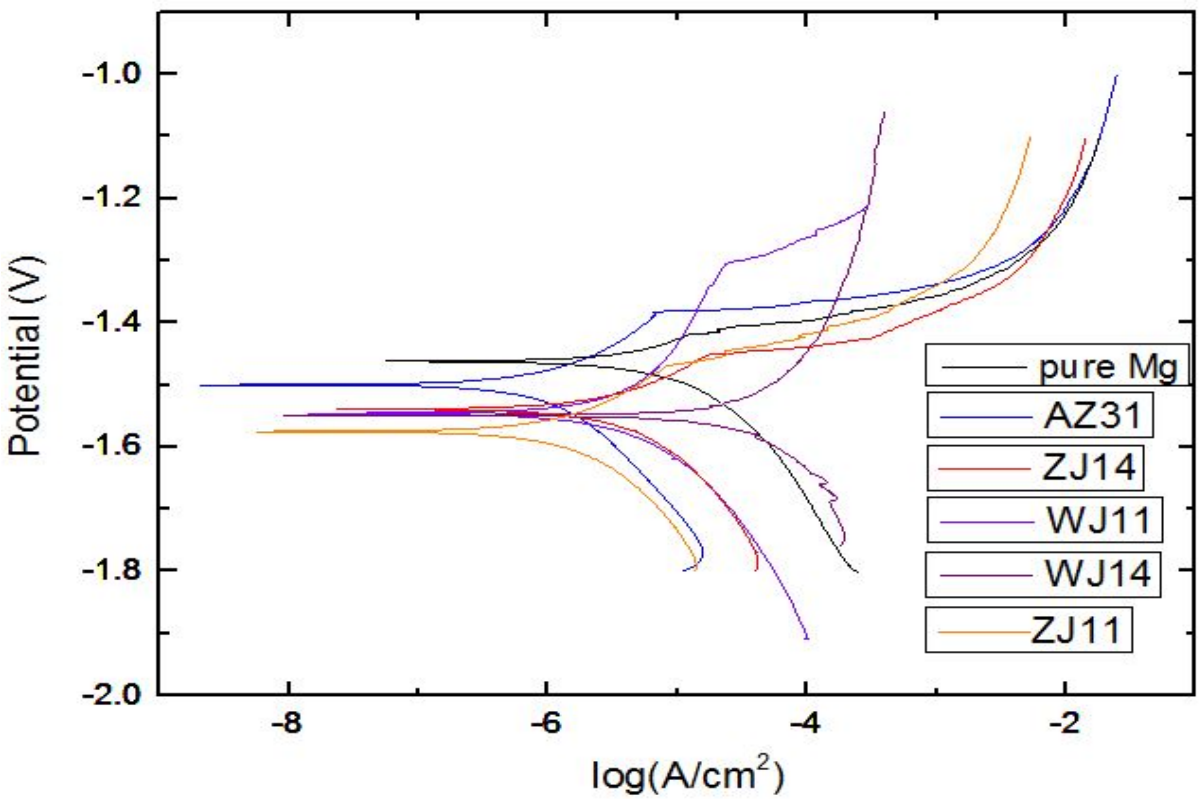

Figure 4.15 Potentiodynamic polarization curves of WJ11, WJ14, ZJ11, ZJ14, AZ31 and pure Mg samples in HBSS.

Table 4.3 Corrosion rates (mm/year) determined by potentiodynamic polarization and immersion techniques of WJ11, WJ14, ZJ11, ZJ14, AZ31 and pure Mg samples in HBSS.

Alloy	Electrochemical measurement			Immersion test
	E_{corr} (V)	i_{corr} ($\mu A/cm^2$)	CR_{corr} (mm/year)	$CR_{7\ days}$ (mm/year)
WJ11	-1.55±0.05	1.41±0.45	0.29±0.09	0.86±0.612
WJ14	-1.56±0.01	5.63±7.33	1.16±1.51	16.68±0.95
ZJ11	-1.57±0.00	0.69±0.06	0.13±0.01	1.38±1.08
ZJ14	-1.51±0.03	5.98±6.78	1.29±1.46	2.47±1.32
AZ31	-1.47±0.03	0.82±0.52	0.18±0.11	0.70±0.1 [36]
Pure Mg	-1.52±0.06	5.05±1.03	1.16±0.24	0.75±0.2 [36]

5.0 DISCUSSION

5.1 Microstructure analysis of Mg-Y-Sr and Mg-Zn-Sr alloys

Zn, Sr, and Y are the common alloying elements for magnesium and have the solution hardening effect on magnesium alloys [31]. The formation of intermetallic compounds, as observed in the x-ray diffraction pattern (Figure 4.1), in a ternary (Mg-Zn-Sr) phase could be further explained by binary phase (Figure 5.1). According to the Mg-Sr binary phase diagram, during solidification stage, α–Mg begins to form first and the liquid phase became increasingly rich in Sr content. Further cooling of the melt thus allows for the precipitation of a $Mg_{17}Sr_2$ secondary phase [32]. Experimentally the formation of an $Mg_{17}Sr_2$ secondary phase along with the α–Mg phase was confirmed by XRD (Figure 4.1). The location and distribution of the secondary phase, $Mg_{17}Sr_2$, was observed by SEM/EDS and confirmed to exist along the grain boundaries (Figure 4.2-4.3).

Increasing Sr percentage to 4 wt.% resulted in the higher secondary phase precipitated along the grain boundaries as shown in Figure 4.2 and 4.3. As different factors contributed to preferential binding and formation of the observed phase, thorough analyses were necessary to validate the formation of intermetallic compounds. First, a comparison of the electronegative values of the alloying elements helped to understand the possible preferential intermetallic compounds. A larger difference in electronegative values liked the formation of intermetallic compounds because of the binding force. For instance, the difference between electronegative values of Sr (0.95) and Zn (1.65) was greater than that between Sr (0.95) and Mg (1.31). Therefore, the excess of Sr at the solid-liquid interface would combine with Zn to form a Zn-Sr intermetallic

compound [33]. With the higher melting point, during the solidification stage, the Zn-Sr phase was pushed to the crystal growth edge of the primary α-Mg phase to restrain the growth of dendrites and lead to the grain refinement [33]. According to Mg-Zn phase diagram, Zn composition at the eutectic point was 51.2 wt.% at 340 °C (Figure 5.2). When the temperature decreased, the eutectoid reaction occurred at 325 °C. During solidification, as the dendrites grew, Zn atoms moved from the edge of solidification to the grain or dendritic boundaries to meet the composition requirements of eutectic reaction. Therefore, the eutectic microstructure of MgZn formed at the grain or the dendritic boundaries. The formation of the MgZn phase was mainly caused by the segregation of alloying elements in the space among dendrites, as the liquid there solidified last and had a higher Zn concentration (Figure 4.3a). However, due to the limited amount of Zn-Sr and Mg-Zn intermetallic phase, there is no their peak showed in the x-ray diffraction pattern (Figure 4.1). From Mg-Y binary phase diagram (Figure 5.3), Y has high solubility in magnesium. Despite a limited amount of Y present in the EDS and SEM images, Y dissolved in the Mg matrix and only seldom elements precipitated along grain boundaries (Figure 4.2). Y can incorporate within the surface film, increase protectiveness of Mg-Y alloy and thereby decrease the corrosion rate [34]. As the grain boundaries possess the higher energy, grain boundaries and the secondary phase were etched by the picral acid solution at the initial stage and removed the second phase along grain boundaries (Figure 4.4-4.5). The strength and corrosion properties of Mg alloys could be improved by precipitation hardening [35]. To minimize the presence of the secondary phase along the grain boundaries, the extrusion of rod followed by squeeze casting should be quenched very rapidly to low temperature. This rapid quenching will prevent the formation and diffusion of the secondary phase along the grain boundaries. This will lead to the formation of fine precipitates of $Mg_{17}Sr_2$ in the α-Mg matrix contributing to improved mechanical properties and likely improving the

corrosion characteristics of both the low and high Sr containing compositions. These studies will be conducted in the future.

Further heat treatments at elevated temperatures will allow for the formation of alloy consisting of uniformly dispersed particles throughout the α–Mg matrix. This process is referred to as "aging" [36]. After the appropriate aging time, the alloy is cooled to room temperature; in this state, the second phase may distribute homogenously in α–Mg matrix. The homogeneously distributed secondary phase due to precipitation hardening has been shown to increase the corrosion resistance of Mg alloys [37].

ICP-OES results of ZJ11 (Table 4.2) possessed similar amount of Mg, Sr, and Zn to the overall EDS spectra results of these elements (Figure 4.3a overall). However, the ICP-OES results of ZJ14 showed a higher Sr content within the bulk material as compared to the Sr content seen on the ZJ14 surface detected by EDS (Figure 4.3b overall). In addition, ICP-OES results of the composition of Mg, Sr, Y, and Ca in WJ11 and WJ14 were different from the EDS results of the surface of these alloys as well (Figure 4.2). The discrepancy in elemental composition as measured by ICP-OES and EDS is due to the fact that ICP-OES measures the elemental composition of the bulk material and does not account for variation within the bulk. However, EDS's elemental analysis is location and spot size dependent, thus non-homogenous samples will have varying EDS spectra throughout the sample.

Further examination of the EDS results indicated that the grain boundaries of all of the alloys not only showed the presence of the $Mg_{17}Sr_2$ secondary phase, but are also rich in Mg (Figure 4.2-4.3). This observation can be explained by the propensity of EDS to be heavily reliant on the magnification as well as spot size of the electron beam. It is possible that the interaction volume of the electron beam was larger than the individual grain boundaries, thus the surrounding

Mg was also part of the interaction volume causing increased Mg content detected. Moreover, it is also possible that fine particulates of pure Mg is trapped in the strontium rich secondary phase located at the grain-boundary owing to the processing conditions and variation in the temperature. As a result, a higher Mg content is detected in the EDS.

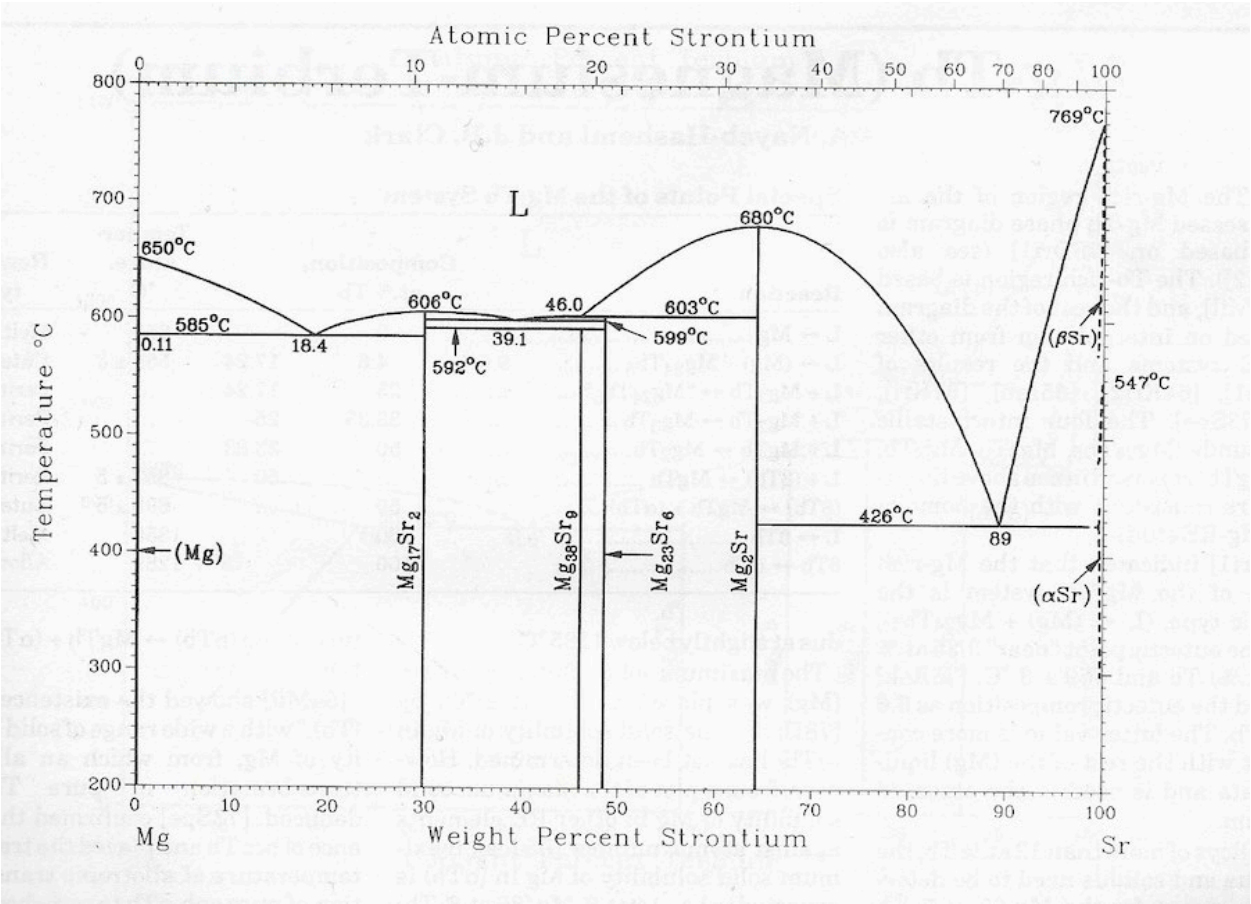

Figure 5.1 Mg-Sr binary phase diagram [32].

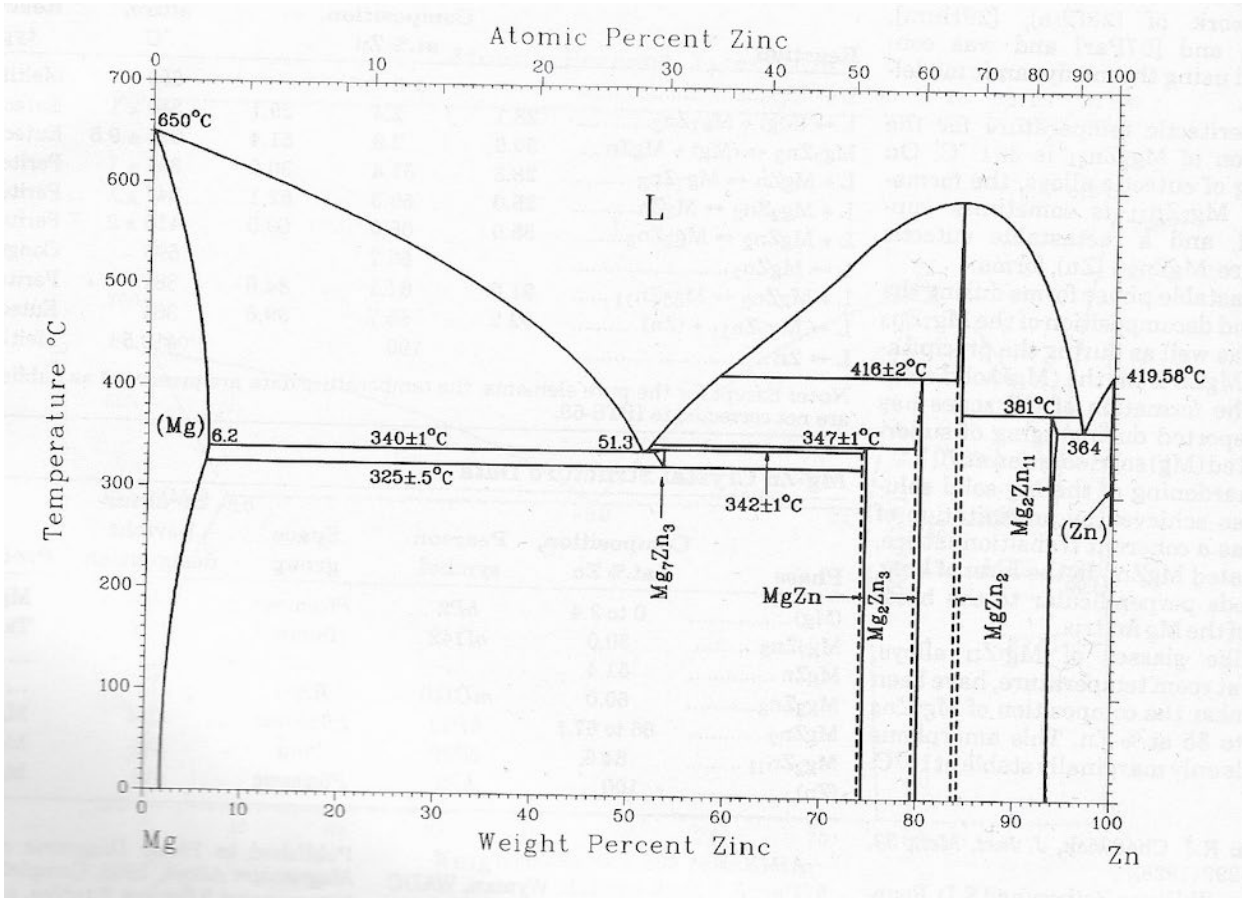

Figure 5.2 Mg-Zn binary phase diagram [32].

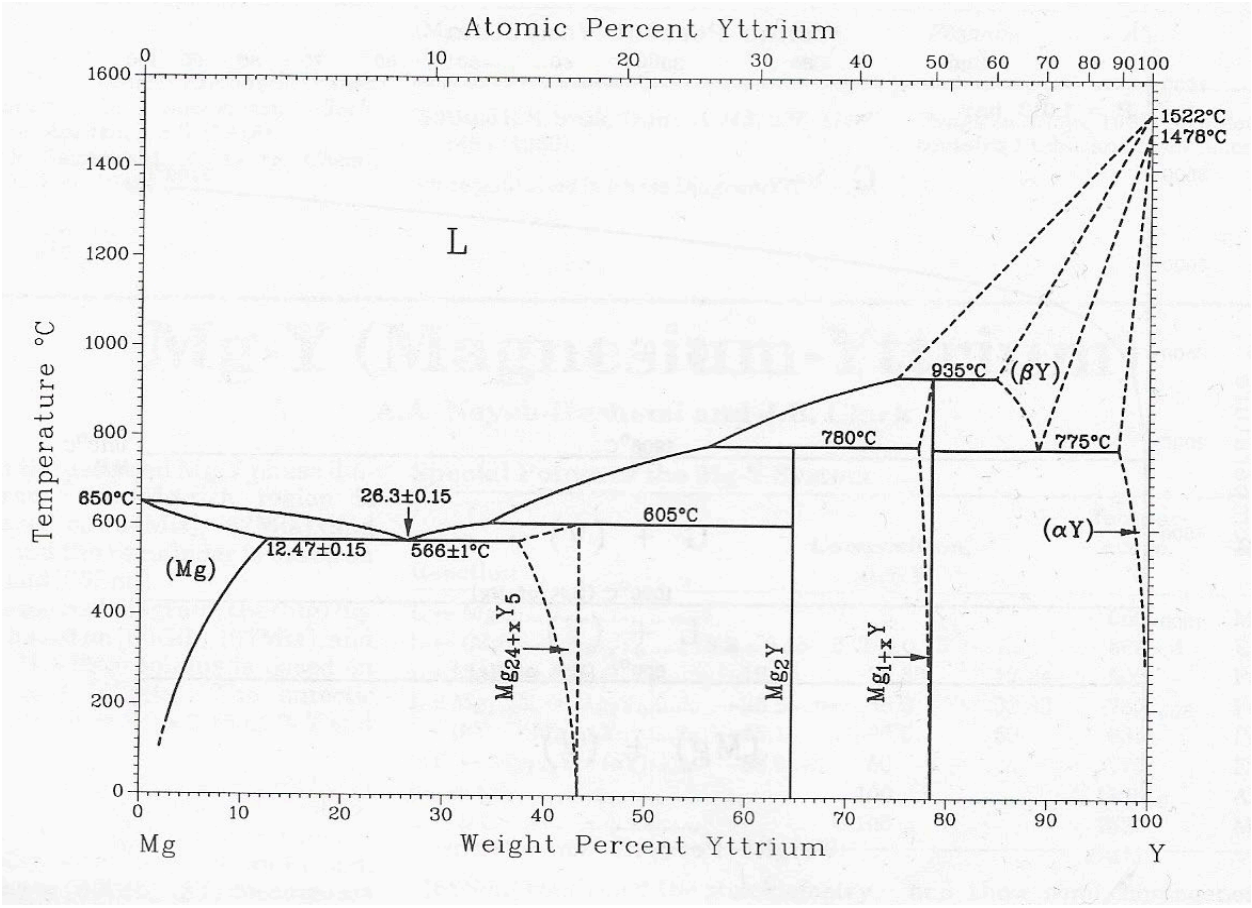

Figure 5.3 Mg-Y binary phase diagram [32].

5.2 Corrosion behavior of Mg-Y-Sr and Mg-Zn-Sr alloys in HBSS

Degradation of the Mg alloys in the HBSS occurred in the alternate mode among galvanic, pitting and crevice corrosion during the prescribed time intervals of immersion. Mg in aqueous solution dissolves according to the following equations:

$Mg_{(s)} \rightarrow Mg^{2+}_{(aq)} + 2e^-$ (anodic reaction)

$2H_2O_{(aq)} + 2e^- \rightarrow H_{2\,(g)} + 2OH^-_{(aq)}$ (cathodic reaction)

$Mg^{2+}_{(aq)} + 2OH^-_{(aq)} \rightarrow Mg(OH)_{2\,(s)}$ (product formation)

In particular, the existence of chloride ion (Cl^-) transforms undissolved $Mg(OH)_2$ into soluble $MgCl_2$, resulting in excess OH^- in the solution [18]. Eventually, the pH values would increase. As a result, when Mg reacts with PO_4^{3-} and Ca^{2+} ions present in the HBSS, a substituted calcium phosphate is nucleated and grow on the Mg surface due to the supersaturated condition at high pH value. In general, the reaction among $H_nPO_4^{(3-n)-}$ (representing various phosphate ions, where n = 0, 1 or 2), Ca^{2+} and Mg^{2+} could be described primarily as [38]:

$H_nPO_4^{(3-n)-} + Ca^{2+} + Mg^{2+} + OH^- \rightarrow Mg_xCa_y(PO_4)_z(OH)$ (product formation). Research has shown that $Mg_xCa_y(PO_4)_z(OH)$ exhibits good biocompatibility [39].

Once the pores are presented on the substrate, the lamellate crystals could grow around them to form grass-like and flower-like morphologies controlled by the number of the pores [40] (as shown in Figure 4.6-4.8). The presence of large holes was due to the pitting corrosion along the grain boundaries which were the second phase precipitates that were more susceptible to attack by Cl^- in the HBSS (Figure 4.9-4.11).

From the immersion corrosion rate measurement (Figure 4.14) it appears that WJ11 alloy degrade slowly at day 7, and slightly increases in corrosion rates at day 21 and day 35. On the other hand, WJ14 alloy degraded rapidly and completely disappeared in 7 days. The corrosion rate of ZJ11 slightly increased with the immersion time. The corrosion rate of ZJ14 does not show any difference at the different time point. Altogether it appears that WJ14 has the highest corrosion rate and there is no difference in corrosion rates among WJ11, ZJ11, and ZJ14, especially at day 7 and day 35. According to previous studies from our group, the corrosion rate at day 7 of pure Mg and AZ31 in HBSS are ~ 0.75 and ~0.70 mmpy, respectively [30]. The corrosion rates of all

Mg alloys studied in this thesis are higher than pure Mg. The pure Mg and AZ31were processed by casting and extrusion and all Mg alloys in this thesis were processed by squeeze casting. Therefore, it appears that processing and post-processing of the alloys have direct influence on the microstructure and hence on the corrosion rate.

5.3 Corrosion results from Tafel plot

The additional of Sr to the Mg alloy lead to an increasing amount of second phase precipitates along the grain boundaries and caused micro-galvanic couple. The precipitates at grain boundaries were less noble than α-Mg matrix. The precipitates were therefore more susceptible to rapid corrosion. A lower corrosion current density means better corrosion resistance. The corrosion current density could be used to estimate the degradation rate of the samples. In Table 3.1, the corrosion rate of ZJ11 in the HBSS is 0.13 ± 0.01 mmpy, which is lower than the ZJ14 alloy (1.29 ± 1.46 mmpy). The corrosion current density of WJ11 is lower than that of WJ14 as well. The corrosion current correlates to the corrosion rate according to Equation 3.2. The addition of higher amount Sr decreased the corrosion resistance of Mg alloy. Owing to the standard electrode reduction potential of Zn (-0.762 V) is higher than Y (-2.38 V) [41], ZJ11 has higher corrosion resistance than WJ11. According to previous studies from our group, the corrosion rate AZ31 and pure Mg are 0.18±0.11 mmpy and 1.16±0.24 mmpy, respectively. The corrosion rate of commercial AZ31 closed to ZJ11 shows good corrosion resistance. The corrosion rate of pure Mg is similar to WJ11and slightly lower than ZJ14. The non-homogeneity in the WJ14 and ZJ14 samples result in the high standard deviation of CR_{corr} in potentiodynamic polarization test.

In general, the anodic branch of polarization curves is characterized by a sudden drop in the anodic current which represented the change in the slope, known as breakdown potential, the lowest potential where corrosion occurs (Figure 4.15). During anodic polarization, a passive film formed on the surface provide a protective layer that made the extent of corrosion damage be minimized. As the potential increase, corrosion via surface breakdown will begin at a certain voltage value termed as the breakdown potential. Breakdown potentials cause the disruption of the passive film and thus expose the bare surface to HBSS contributing to the accelerated corrosion of the alloy.

6.0 CONCLUSIONS AND FUTURE WORK

In this thesis, the following alloys WJ11 (Mg-1 wt. %Y-1 wt.% Sr), WJ14 (Mg-1 wt. %Y-4 wt.% Sr), ZJ11 (Mg-1 wt.%Zn-1 wt.%Sr) and ZJ14 (Mg- 1 wt.% Zn-4 wt.% Sr) alloys were investigated as potential degradable alloys for biomedical application. The squeeze casted alloys were fabricated by melting in an electric resistance furnace with unidirectional force of 200 MPa on the melt. X-ray diffraction patterns of each alloy exhibited α-Mg phase, and ZJ14 and WJ14 showed the presence of $Mg_{17}Sr_2$ intermetallic phase. In addition, scanning electron microscopy-EDS showed that the second phase grew along the grain boundaries for all of the alloys. The addition of Sr in Mg alloys leads to the refinement of the grains and grain size decreases with an increase in Sr content. The corrosion rates of WJ11, ZJ11, and ZJ14 did not exhibit any difference at day 7 and day 35 as determined by immersion corrosion tests. However, WJ14 alloy samples degraded much more rapidly and disintegrated into fragments within 7 days of exposure to HBSS. Potentiodynamic polarization test in HBSS showed that the corrosion rate of ZJ11 was the lowest among Mg-Zn-Sr, Mg-Y-Sr and pure Mg under the same condition; however, it was similar to AZ31. Further addition of Sr to 4% adversely affected the corrosion resistance of the Mg-Zn-Sr, Mg-Y-Sr alloys. Precipitation hardening could be employed with these Mg alloys to enhance their corrosion properties as well as mechanical properties in the future. Moreover, various coating technologies, such as metal on metal coatings, plasma spray, chemical vapor deposition, pulsed laser deposition, ion beam assisted deposition, solution coatings, electrodeposition and conversion coating, can be further employed to decrease the corrosion rate and potentially improve the bioactivity of these alloys [42]. Future testing would include both biomechanical testing as well as *in-vitro* cytocompatibility studies. For future *in-vitro* cytocompatibility studies, the pre-osteoblast

MC3T3 cell line would be used to evaluate the alloys' influence on cell attachment, survival, and proliferation. These studies are planned for in the future.

BIBLIOGRAPHY

[1] S. De, "U.S. Orthopedic Devices Market to Witness Massive Growth Over 2017-2024," 2018. .

[2] M. Navarro, A. Michiardi, O. Castan, and J. A. Planell, "Biomaterials in orthopaedics," no. July, pp. 1137–1158, 2008.

[3] S. Jin *et al.*, "Journal of Colloid and Interface Science Development of a three-dimensionally printed scaffold grafted with bone forming peptide-1 for enhanced bone regeneration with in vitro and in vivo evaluations," *J. Colloid Interface Sci.*, vol. 539, pp. 468–480, 2019.

[4] S. Y. Kim, Y. K. Kim, Y. Kwang-kyun, K. B. Lee, and M. ho Lee, "Determination of ideal Mg–35Zn–xCa alloy depending on Ca concentration for biomaterials," *J. Alloys Compd.*, vol. 766, pp. 994–1002, 2018.

[5] SSA El-Rahman, "Neuropathology of aluminum toxicity in rats (glutamate and GABA impairment)," *Pharmacol. Res.*, vol. 47, pp. 189–194, 2003.

[6] M. P. Staiger, A. M. Pietak, J. Huadmai, and G. Dias, "Magnesium and its alloys as orthopedic biomaterials: A review," *Biomaterials*, vol. 27, no. 9, pp. 1728–1734, 2006.

[7] L. S. Nair and C. T. Laurencin, "Biodegradable polymers as biomaterials," *Prog. Polym. Sci.*, vol. 32, no. 8–9, pp. 762–798, 2007.

[8] M. Vallet-Regí and J. M. González-Calbet, "Calcium phosphates as substitution of bone tissues," *Prog. Solid State Chem.*, vol. 32, no. 1–2, pp. 1–31, 2004.

[9] L. L. Hench, "The story of Bioglass," pp. 967–978, 2006.

[10] S. V. Dorozhkin, "Bioceramics of calcium orthophosphates," *Biomaterials*, vol. 31, no. 7, pp. 1465–1485, 2010.

[11] D. Liu, D. Yang, X. Li, and S. Hu, "Mechanical properties, corrosion resistance and biocompatibilities of degradable Mg-RE alloys: A review," *J. Mater. Res. Technol.*, no. x x, pp. 1–12, 2018.

[12] C. A. Baker H, *ASM Specialty Handbook: Magnesium and Magnesium Alloys*. ASM International, 1999.

[13] D.-T. Chou, "Fundamental study of the development and evalution of biodegradable Mg-Y-Ca-Zr alloys as novel implant materials," University of Pittsburgh, 2015.

[14] L. E. Claes, “Mechanical characterization of biodegradable implants,” *Clin. Mater.*, vol. 10, no. 1–2, pp. 41–46, Jan. 1992.

[15] M. Knapek, P. Minárik, J. Čapek, R. Král, J. Kubásek, and F. Chmelík, “Corrosion of pure magnesium and a WE43 magnesium alloy studied by advanced acoustic emission analysis,” *Corros. Sci.*, vol. 145, no. June, pp. 10–15, 2018.

[16] G. Song and A. Atrens, “Understanding magnesium corrosion. A framework for improved alloy performance,” *Adv. Eng. Mater.*, vol. 5, no. 12, pp. 837–858, 2003.

[17] Y. Xin, T. Hu, and P. K. Chu, “Acta Biomaterialia In vitro studies of biomedical magnesium alloys in a simulated physiological environment : A review,” vol. 7, pp. 1452–1459, 2011.

[18] Z. Li, X. Gu, S. Lou, and Y. Zheng, “The development of binary Mg-Ca alloys for use as biodegradable materials within bone,” *Biomaterials*, vol. 29, no. 10, pp. 1329–1344, 2008.

[19] W. Mueller, M. L. Nascimento, M. Fernández, and L. De Mele, “Acta Biomaterialia Critical discussion of the results from different corrosion studies of Mg and Mg alloys for biomaterial applications q,” *Acta Biomater.*, vol. 6, no. 5, pp. 1749–1755, 2010.

[20] V. K. Bommala, M. G. Krishna, and C. T. Rao, “Magnesium matrix composites for biomedical applications: A review,” *J. Magnes. Alloy.*, no. xxxx, pp. 1–8, 2018.

[21] N. E. L. Saris, E. Mervaala, H. Karppanen, J. A. Khawaja, and A. Lewenstam, “Magnesium: An update on physiological, clinical and analytical aspects,” *Clin. Chim. Acta*, vol. 294, no. 1–2, pp. 1–26, 2000.

[22] Z. G. Huan, M. A. Leeflang, J. Zhou, L. E. Fratila-Apachitei, and J. Duszczyk, “In vitro degradation behavior and cytocompatibility of Mg-Zn-Zr alloys,” *J. Mater. Sci. Mater. Med.*, vol. 21, no. 9, pp. 2623–2635, 2010.

[23] J. Y. Lee, H. K. Lim, D. H. Kim, W. T. Kim, and D. H. Kim, “Effect of volume fraction of qusicrystal on the mechanical properties of quasicrystal-reinforced Mg-Zn-Y alloys,” *Mater. Sci. Eng. A*, vol. 448–451, pp. 987–990, 2007.

[24] B. VM., “Effect of zirconium on the grain size of magnesium containing 4.5% Zn,” *Met. Sci. Heat Treat.*, vol. 5, no. 9, pp. 543–544, 1963.

[25] L. Jiang, M. Multigner, A. Me, J. L. Gonza, L. Munuera, and N. Vilaboa, “In vitro biocompatibility of an ultrafine grained zirconium,” vol. 28, pp. 4343–4354, 2007.

[26] X. Zeng, Y. Wang, W. Ding, A. A. Luo, and A. K. Sachdev, “Effect of Strontium on the Microstructure , Mechanical Properties , and Fracture Behavior of AZ31 Magnesium Alloy,” vol. 37, no. April, 2006.

[27] C. Liu, L. Tan, Y. Zhao, P. Wan, H. Pan, and X. Zhao, *In Vitro Cytocompatibility and Osteogenic Potential of Biodegradable Mg – Sr Alloys*. Springer Singapore, 2018.

[28] A. D. Sudholz, K. Gusieva, X. B. Chen, B. C. Muddle, M. A. Gibson, and N. Birbilis, "Electrochemical behaviour and corrosion of Mg – Y alloys," *Corros. Sci.*, vol. 53, no. 6, pp. 2277–2282, 2011.

[29] M. Bornapour, N. Muja, D. Shum-tim, M. Cerruti, and M. Pekguleryuz, "Acta Biomaterialia Biocompatibility and biodegradability of Mg – Sr alloys : The formation of Sr-substituted hydroxyapatite q," *Acta Biomater.*, vol. 9, no. 2, pp. 5319–5330, 2013.

[30] D. Hong, "Fundamental study of the design and development of magnesium-zinc based alloys for biodegradable implant devices," University of Pittsburgh, 2015.

[31] B. M. HE Friedrich, *Magnesium technology – metallurgy, design data, applications*. Berlin: Springer, 2006.

[32] L. K. Thaddeus B. Massalski, Hiroaki Okamoto, P.R. Subramanian, *Binary alloy phase diagrams*, 2nd ed. Materials Park, Ohio : ASM International, c1990.

[33] R. Guan *et al.*, "Development and evaluation of a magnesium – zinc – strontium alloy for biomedical applications — Alloy processing , microstructure , mechanical properties , and biodegradation," *Mater. Sci. Eng. C*, vol. 33, no. 7, pp. 3661–3669, 2013.

[34] A. C. Hänzi, P. Gunde, M. Schinhammer, and P. J. Uggowitzer, "On the biodegradation performance of an Mg-Y-RE alloy with various surface conditions in simulated body fluid," *Acta Biomater.*, vol. 5, no. 1, pp. 162–171, 2009.

[35] Q. Peng *et al.*, "Degradation behavior of Mg-based biomaterials containing different long-period stacking ordered phases," *Sci. Rep.*, vol. 4, pp. 1–9, 2014.

[36] J. William D. Callister, *Materials Science and Engineering An Introduction*. John Wiley & Sons, Inc., 2007.

[37] L. M. Peng, J. W. Chang, X. W. Guo, A. Atrens, W. J. Ding, and Y. H. Peng, "Influence of heat treatment and microstructure on the corrosion of magnesium alloy Mg-10Gd-3Y-0.4Zr," *J. Appl. Electrochem.*, vol. 39, no. 6, pp. 913–920, 2009.

[38] S. Zhang *et al.*, "Research on an Mg-Zn alloy as a degradable biomaterial," *Acta Biomater.*, vol. 6, no. 2, pp. 626–640, 2010.

[39] F. Witte, V. Kaese, H. Haferkamp, E. Switzer, and A. Meyer-lindenberg, "In vivo corrosion of four magnesium alloys and the associated bone response," vol. 26, pp. 3557–3563, 2005.

[40] J. Yang, Y. Jiao, Q. Yin, Y. Zhang, and T. Zhang, "Calcium phosphate coating on magnesium alloy by biomimetic method : Investigation of morphology , composition and formation process," vol. 2, no. 2, pp. 149–155, 2008.

[41] D. C. Harris, *Quantitative Chemical Analysis*, Seventh. 2007.

[42] N. T. Kirkland, “Magnesium biomaterials: past, present and future,” *Corros. Eng. Sci. Technol.*, vol. 47, no. 5, pp. 322–328, 2012.